INTERNATIONAL JOURNAL FOR NUMERICAL METHODS IN FLUIDS
*Int. J. Numer. Meth. Fluids* 2010; **62**:1264–1298
Published online 21 May 2009 in Wiley InterScience (www.interscience.wiley.com). DOI: 10.1002/fld.2064

# Modeling of lifting-device aerodynamics using the actuator surface concept

Christophe Sibuet Watters*, † and Christian Masson

*Department of Mechanical Engineering, École de Technologie Supérieure, 1100, rue Notre-Dame Ouest, Montréal (Québec), Canada H3C1K3*

SUMMARY

The actuator surface (AS) concept and its implementation within a differential, Navier–Stokes control volume finite-element method (CVFEM) are presented in this article. Inspired by vortex and actuator disk methods, the AS concept consists of using porous surfaces carrying velocity and pressure discontinuities to model the action of lifting surfaces on the flow. The underlying principles and mathematics associated with AS are first reviewed, as well as their implementation in a CVFEM. Results are presented for idealized 2D cases with analytical solutions, as well as for the 3D cases of a finite wing and an experimental wind turbine. In the case of the finite wing, wake induction is well handled by the model with accurate predictions of induced angles and drag when compared with the Prandtl lifting line model. Comparisons with volume force approaches, often used to model the action of propellers or wind turbine blades in a simplified analysis, show that the AS concept has some interesting advantages in terms of accuracy and respect of flow physics. This new approach is easy and rapid to embed in most computational fluid dynamics (CFD) methods. It is applicable to a wide range of problems involving thin lifting devices like finite wings, propellers, helicopter or wind turbine blades. Copyright © 2009 John Wiley & Sons, Ltd.

Received 30 September 2008; Revised 16 March 2009; Accepted 20 March 2009

KEY WORDS: control volume finite-element methods; CFD; actuator surface; actuator disk; wake induction; finite wings; rotating flows

## 1. INTRODUCTION

As widely illustrated in the computational fluid dynamics (CFD) literature, for a variety of complex mechanical systems where the level of physical detail is either unrealizable or unnecessary, CFD simulations make use of distributed volume forces to represent the action of fans [1], propellers [2], helicopter [3–6] or wind turbine blades [7], or even bluff bodies [8]. The prescription of volumes

*Correspondence to: Christophe Sibuet Watters, Department of Mechanical Engineering, École de Technologie Supérieure, 1100, rue Notre-Dame Ouest, Montréal (Québec), Canada H3C13K.
†E-mail: christophe.sibuet@etsmtl.ca

Contract/grant sponsor: Canada Research Chairs Program
Contract/grant sponsor: Natural Sciences and Engineering Research Council of Canada (NSERC)

and force distributions acting within them is important issues that can strongly influence the flow solution. With regards to fans or propellers, the actuator disk concept introduced by Froude should also be included in this group of simplified models; however, the action of the modeled device is spread over a surface rather than a volume. Volume forces become surface forces and discontinuities occur at the actuator disk surface in flow properties like pressure and velocity (see for example [9]). Inspired by the actuator disk concept, this article proposes the use of a new type of singular surface, called an actuator surface (AS), to represent the action of any lifting surface within a differential Navier–Stokes, control volume (CV) finite-element-based method. An AS is simply a geometric surface carrying velocity and pressure discontinuities, as well as surface forces, which are all determined from the circulation along the lifting sections of the AS. Equivalently, an AS is a porous vortex sheet that represents the bound vorticity system of a lifting device. The flow induced by the AS is solved using a CFD method that has been adapted to account for the kinematic and dynamic influence of the AS. As for volume force approaches, the trailing system of vorticity is naturally modeled by the CFD method. To situate the AS approach, Figure 1 presents a possible classification of models for lifting-device aerodynamics by sketching different approaches to model e.g. a lifting wing. On the left part of the figure, vortex models regroup lifting-line, vortex–lattice and panel models. These models are based on distributions of vorticity singularities whose magnitudes are set either based on kinematic conditions (surface tangency) or from blade-element analysis (in the case of the lifting-line approach). On the right part of the figure, approaches are regrouped under the 'finite-element models' banner to point out that their underlying principles consist of solving the differential equations describing the flow (the Navier–Stokes equations) using a CFD methodology. The 'Navier–Stokes' approach consists of the use of a CFD approach to model the flow around the wing where the wing is modeled by its

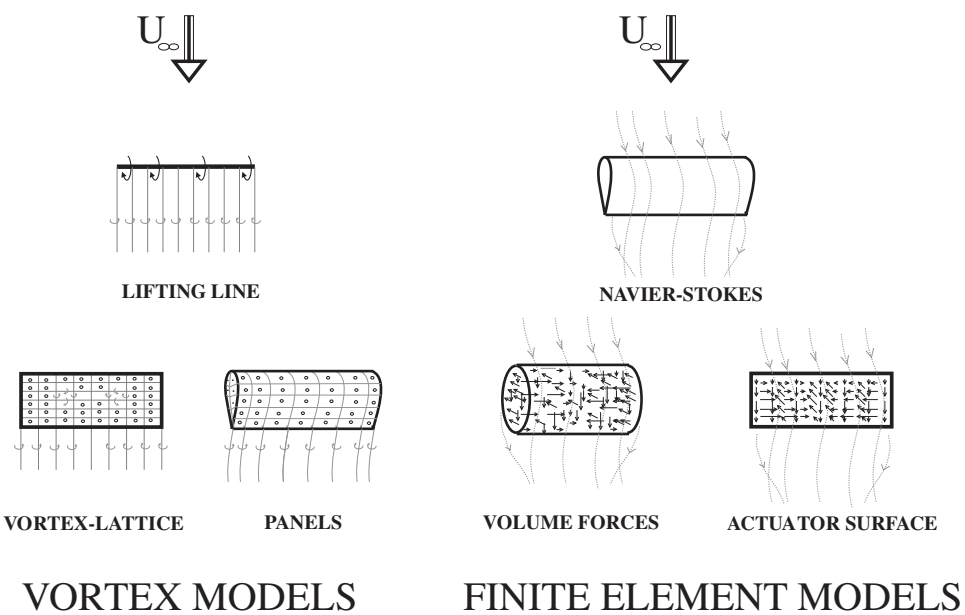


Figure 1. Schematic representation of aerodynamic models for a lifting wing.



DOI: 10.1002/fld

true geometry and a no-slip (or tangency) condition at its surface. On another level, volume force and AS approaches model the wing either by a volume or an AS that do not exactly spouse the true wing geometry. A system of forces is prescribed to represent the action of the wing on the flow, whose magnitude is evaluated using local blade-element analysis. As will be shown, the AS represents a potentially interesting concept to add to CFD methodologies with relative advantages over volume force approaches. Indeed, the action of the modeled device is spread over a surface rather than a volume, preventing arbitrary choices of volume thickness and force distributions with subsequent dependency on the flow solution or computational instabilities. Furthermore, the AS is perfectly compatible with the vorticity principles of creation and evolution of vortices, and the Kutta–Joukowski theorem for lift production, whereas volume force approaches fail to always comply with such principles and as a consequence, may not reproduce the genuine characteristics of the flow.

This article is divided into three sections: (1) description of the mathematical model for the AS, (2) description of the numerical method and of its necessary adaptations to include the AS model and (3) presentation of results obtained using this new concept. The results focus on the validation of the AS concept with 2D and 3D situations having analytical solutions. As a final demonstration, the case of wind turbine aerodynamics is studied by using rotating ASs. Comparisons with either analytical or experimental results and with results from volume force approaches are made to gain insight into the capabilities of the AS concept.

## 2. MATHEMATICAL ASPECTS OF ASs

The theories presented in the following sections are taken from classical concepts of incompressible fluid mechanics. The original idea presented concerns the introduction of the AS defined as a porous surface of velocity and pressure discontinuities in the flow, to represent the action of a lifting device. Two conditions are imposed in the AS definition to guarantee vorticity flux conservation and the absence of energy exchange in the process of lift creation for inviscid flows. These two conditions are sufficient to fix the kinematic and dynamic influence of the AS on the flow.

### *2.1. ASs: implications*

Figure 2 shows a simple model of a rectangular AS, fixed and immersed in an oncoming uniform flow, which can be used for the analysis of finite-wing aerodynamics. Streamlines and contour plots of pressure jumps across the AS are drawn to illustrate qualitatively the typical action of an AS on the flow. A cartesian $(X, Y, Z)$ axis is defined so that the $X$ axis points in the flow direction and the AS is a flat surface perpendicular to the $Z$ direction, lying in a plane of equation $z = Z_P$. By convention, the discontinuities occur in the $Z$ direction, which means that the discontinuity of a variable $\phi$ ($\phi$ is alternatively $u, v, w$ or $p$, the flow velocity components and pressure) is measured as

$$\Delta\phi = \phi_{Z_P+} - \phi_{Z_P-} \tag{1}$$

where implicitly, the jump $\Delta\phi$ is a function of the location $X, Y$ on the AS and where $\phi_{Z_P+}$ and $\phi_{Z_P-}$ are the limit values of the flow characteristics on both sides of the AS:

$$\phi_{Z_P+} = \lim_{z \to z_P+, z > z_P} \phi, \quad \phi_{Z_P-} = \lim_{z \to z_P-, z < z_P} \phi \tag{2}$$



DOI: 10.1002/fld

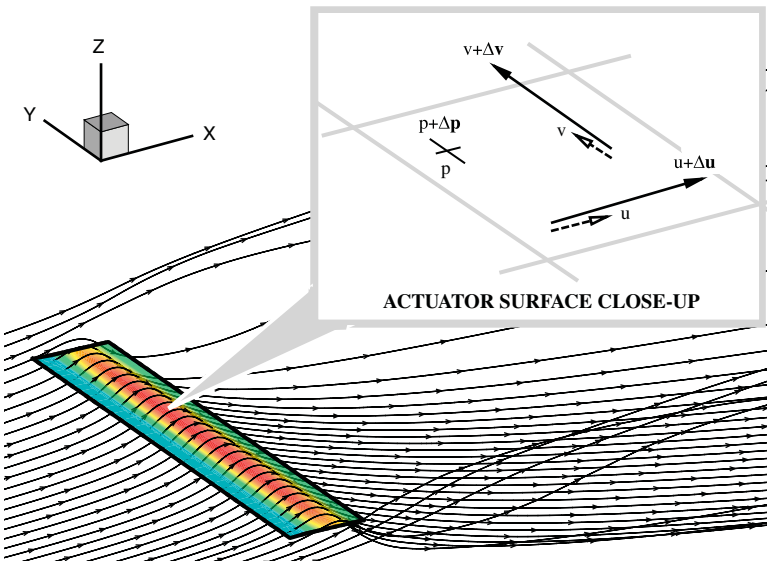


Figure 2. A simple actuator surface.

*As a first condition*, we require that the AS respects the condition of zero net flux of vorticity for any CV that intersects the AS surface. For the AS of Figure 2, this is reflected by the following constraint on the flow velocity discontinuities $\Delta u$ and $\Delta v$:

$$\frac{\partial \Delta v}{\partial x} - \frac{\partial \Delta u}{\partial y} = 0 \tag{3}$$

This constraint ensures that the circulation of the velocity jump around any closed contour $C$ drawn on the AS is null, since from Green's theorem

$$\int_C \Delta u \delta x + \Delta v \delta y = \int_D \left( \frac{\partial \Delta v}{\partial x} - \frac{\partial \Delta u}{\partial y} \right) \delta A = 0$$

where $D$ is the region bounded by $C$. Equation (3) guarantees that the vertical component of the vorticity through the AS is continuous, hence the net flux of vorticity for any CV that intersects the AS is null. This constraint finds its equivalent in vortex models, when analyzing the bound and trailing systems of vorticity and where the trailing vorticity is linked to the spanwise variations of the bound vorticity using the principles of vorticity conservation. In vortex models in addition, vorticity must be modeled explicitly in the wake whereas here, the flow around the AS is solved using a finite-volume CFD method, which implicitly accounts for the wake dynamics.

From the point of view of dynamics, since the AS is porous, when a fluid particle crosses it, the particle momentum undergoes a sudden variation, which must be explained by a set of impulsive forces attached to the AS. In the direction tangent to the AS, the expression of these forces (per unit surface area) is given by the product of the mass flux through the AS and the velocity discontinuities, in this case

$$f_X = \rho w_{\mathrm{av}} \Delta u \quad \text{and} \quad f_Y = \rho w_{\mathrm{av}} \Delta v \tag{4}$$



DOI: 10.1002/fld

where the suffix *av* indicates that the value considered for the $w$ component is an average of the component limit values on both sides of the AS (in the particular case of the vertical component, $\Delta w = 0$ for mass conservation reasons and $w$ is continuous through the AS). For the axial flow velocity component $u$, the expression of $u_{\text{av}}$ is:

$$u_{\text{av}} = \frac{u_{Z_P-} + u_{Z_P+}}{2} = u_{Z_P-} + \frac{\Delta u}{2} = u_{Z_P+} - \frac{\Delta u}{2} \tag{5}$$

*As a second condition* in the AS definition, we now require that the attached system of forces does not exert a mechanical work on the flow, i.e. $f_X u_{\text{av}} + f_Y v_{\text{av}} + f_Z w_{\text{av}} = 0$. This condition is in agreement with the action of the AS modeling only processes linked to lift generation, which by definition is perpendicular to the local velocity. From this constraint, we deduce the expression of $f_Z$ as:

$$f_Z = -\rho(u_{\text{av}}\Delta u + v_{\text{av}}\Delta v) \tag{6}$$

The normal component $f_Z$ implies that there must exist a pressure jump at the AS to balance for this normal component, whose magnitude is exactly equal to $f_Z$, hence it is found that: $\Delta p = f_Z$. Equation (6) is a Bernoulli type equation and ensures that total pressure is constant on both sides of the AS. It is indeed easy to verify that:

$$p_{Z_P-} + \tfrac{1}{2}\rho(u^2_{Z_P-} + v^2_{Z_P-} + w^2_{Z_P-}) = p_{Z_P+} + \Delta p + \tfrac{1}{2}\rho(u^2_{Z_P+} + v^2_{Z_P+} + w^2_{Z_P+})$$

Generalizing the AS mathematical description to the case of moving ASs or to ASs of different shapes than the flat surface is straightforward when considering the vorticity vector associated with the AS. Calling $\Delta\mathbf{V}$ the vector associated with the velocity discontinuity of the AS, and $\mathbf{n}_{\text{AS}}$ the unit vector normal to the AS at the point where we examine the AS action on the flow, the AS is also a vortex sheet of intensity described by the vorticity vector $\boldsymbol{\gamma} = \mathbf{n}_{\text{AS}} \times \Delta\mathbf{V}$. The first condition that was set on the AS in Equation (3) can be generalized as a condition on the divergence of the vorticity vector:

$$\nabla \cdot \boldsymbol{\gamma} = 0 \tag{7}$$

Turning to the AS dynamic action on the flow, it is found that in the general case, the attached system of force, per unit area of the AS, is given by a relation of the Kutta–Joukowski type

$$\mathbf{f} = -\rho \mathbf{V}_{\text{av,rel}} \times \boldsymbol{\gamma} \tag{8}$$

where $\mathbf{V}_{\text{av,rel}}$ is the average flow velocity measured relative to the AS: $\mathbf{V}_{\text{av,rel}} = \mathbf{V}_{\text{av}} - \mathbf{V}_{\text{AS}}$ and $\mathbf{V}_{\text{AS}}$ is the velocity of the AS at the location where the force is evaluated which, in the general case, might not be null (moving or deforming AS). Equation (8) expresses that in a reference frame where the AS appears fixed, total pressure is constant across the AS since the Navier–Stokes equations, once recast under the form $\nabla H = \rho \mathbf{V}_{\text{rel}} \times \boldsymbol{\omega} + \mathbf{f}'$, and after integration across the AS, gives $\Delta H = (\rho \mathbf{V}_{\text{av,rel}} \times \boldsymbol{\gamma} + \mathbf{f}) \cdot \mathbf{n}_{\text{AS}} = 0$ (where $H$ is the total pressure, $\boldsymbol{\omega}$ is the flow vorticity and $\mathbf{f}'$ corresponds to the density of the external force). It is worth mentioning that the form of Equations (7) and (8) guarantees that the modeled action of the AS on the flow is independent of the convention used to identify the two sides (lower and upper) of the AS and guarantees invariance of the formulation with respect to frame of reference or choices of system coordinates.

If the AS is analyzed in an inertial frame of reference where it is not moving ($\mathbf{V}_{\text{AS}} = 0$), then no power is transferred between the flow and the AS. In the general case of a moving AS, it is



DOI: 10.1002/fld

trivial to demonstrate from Equation (8) that $\mathbf{f}\cdot\mathbf{V}_{\mathrm{av,rel}}=0$. Rewriting this last equation by adding the term $\mathbf{f}\cdot\mathbf{V}_{\mathrm{AS}}$ on each side raises $\mathbf{f}\cdot(\mathbf{V}_{\mathrm{av}}+\mathbf{V}_{\mathrm{AS}})=\mathbf{f}\cdot\mathbf{V}_{\mathrm{AS}}$ where the vector sum $\mathbf{V}=\mathbf{V}_{\mathrm{av}}+\mathbf{V}_{\mathrm{AS}}$ corresponds in fact to the absolute average flow velocity at the AS. This yields:

$$\mathbf{f}\cdot\mathbf{V}=\mathbf{f}\cdot\mathbf{V}_{\mathrm{AS}} \tag{9}$$

This last identity means that the mechanical power transmitted by the AS to the flow (the left part of the equation) is equal to the power it takes to keep the AS in motion (the right part). The case of the finite wing is rich in learnings: the integration of all surface forces results in a total force exerted by the AS on the flow where the vertical component is the lift, and the horizontal is the induced drag. In inviscid flow, a fixed wing does not produce nor dissipates energy within the fluid, however, a moving one encounters an induced drag force, which necessitates an external source of energy. This energy serves to continuously create, when advancing, the vortical wake: this is the price to pay to create vorticity in inviscid flows. When they occur, exchange of energy between the AS and the flow happen exclusively on the AS, since the wake is assumed to be a free vortex sheet and therefore cannot exchange energy with the flow [10].

Although developed in agreement with basic fluid mechanics principles, the AS is a singular vortex sheet since it is allowed to be porous to the flow. From Helmholtz laws, we would expect a vortex sheet that represents a lifting surface to lie along flow streamlines, with induced velocity and pressure discontinuities given by $\Delta\mathbf{V}=\boldsymbol{\gamma}\times\mathbf{n}_{\mathrm{AS}}$ and $\Delta p=-\rho\mathbf{V}_{\mathrm{av,rel}}\cdot\Delta\mathbf{V}$ as found in textbooks [10, 11]. The condition on the vortex sheet that it must lie on the flow streamlines would in fact be a sufficient condition to fix the vortex sheet intensity and deduce its action on the flow. Here however, the intent is not to deduce the AS intensity from a consideration of the flow tangency, but rather to impose a distribution of velocity discontinuity on the AS surface that represents a known distribution of circulation along the span of a lifting device. Fixing the distribution of circulation along the span is achieved using blade-element analysis, as presented in the following section.

Although developed according to inviscid flow theory, the AS concept can be integrated into any Navier–Stokes solver able to model for viscosity (and eventually turbulence) effects in the flow under analysis. However, the AS as presented here is unable to model the action of viscosity that would occur in boundary layers, and therefore viscous drag of a body cannot be modeled. As with vortex flow models, the AS focuses on the modeling of vorticity in the flow, and therefore of wake induction effects on lifting-device aerodynamics.

### 2.2. *Blade-element analysis*

Blade-element analysis is used to determine the values of circulation along sections of a lifting wing (either in translation or rotation) to be modeled using the AS concept. Figure 3 presents a sketch of a wing section of chord length $c$, where the incoming flow experienced by the airfoil corresponds to the relative velocity $\mathbf{V}_{\mathrm{av}}$ as presented in the previous section. Once the local flowfield characteristics are known, as well as wing geometrical (twist and chord distributions) and operational (pitch angle, motion of the wing) characteristics, it is possible to calculate the local angle of attack $\alpha$ of the incoming flow. Using the Kutta–Joukowski theorem, the following expression for the circulation of velocity around the airfoil $\Gamma$ can be found:

$$\Gamma=\tfrac{1}{2}c\|\mathbf{V}_{\mathrm{rel}}\|C_l \tag{10}$$

where $C_l$ is the lift coefficient of the airfoil defining the blade section, a function of the relative angle of attack $\alpha$ and the local Reynolds number. Note that these equations deviate from the classical



DOI: 10.1002/fld

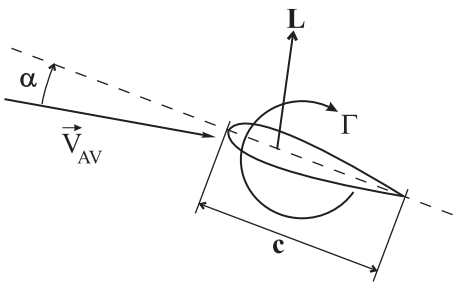


Figure 3. Cross section of a wing.

equations found in textbooks [12], since here the local velocity $\mathbf{V}_{\text{rel}}$ is used instead of the usual (often uniform) inflow velocity $U_\infty$ found far upstream. The formal proof of the Kutta–Joukowski theorem is indeed often presented for 2D irrotational flows whereas here we are confronted with 3D inviscid flows that can be rotational. The derivation leading to Equation (10), valid for 2D irrotational flows, is here assumed to apply in the case of the AS. Schmitz and Chattot [13] have studied this hypothesis using a coupled Navier–Stokes/vortex-panel solver for the study of wind turbine aerodynamics and have found that deviations from Equation (10) are to the order of a few percents, especially when the blade is experiencing stall. In practice, the evaluation of $\mathbf{V}_{\text{av}}$ can be made on the wing or at some location upstream; Vortex methods [3] that are based on lifting lines usually estimate the wing bound circulation from Equation (10).

### *2.3. Distribution of discontinuities on planar AS*

Once the circulation $\Gamma$ around a section of a planar AS is known, the task consists of distributing this circulation along the section in the most appropriate way. The line integral of $\Delta u$ along a cross section must be equal to the circulation $\Gamma$ around this section. For the singular surface of Figure 2, calling $c$ the chord length of one section, this can be mathematically expressed as:

$$\int_0^c \Delta u \, \mathrm{d}x = \Gamma \quad \text{along a line } (z = z_P;\ y = y_{\text{line}})$$

The constant distribution $\Delta u = \Gamma/c$ is the simplest but performs poorly since it sets rapid variations of the $\Delta u$ field, which are hard to manage numerically without instabilities in the flow solution. Distributions respecting continuity of $\Delta u(x, y, z)$ are more appropriate. In this work, a simple parabolic distribution is assumed

$$\Delta u_P = \frac{6\Gamma}{c^3} x_P (c - x_P) \tag{11}$$

where $x_P$ is the distance from a point P on the AS to the leading edge of the wing along the $x$-axis direction, as shown in Figure 4.

Shen *et al.* [14] and Dobrev *et al.* [15], who use AS models to study wind turbine aerodynamics, where the AS is a surface of pressure discontinuity only, have used more sophisticated distributions, which are based on the actual, inviscid distributions occurring around the airfoils defining the blades (Shen *et al*. have limited their analysis to 2D problems). These distributions are therefore functions of the airfoil profile, the angle of attack and the Reynolds number. In this article, the



DOI: 10.1002/fld

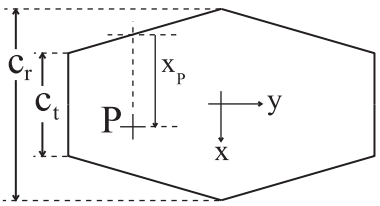


Figure 4. Flat surface modeling the tapered wing.

parabolic distribution proved to be simple and effective as demonstrated by the results obtained and presented in Section 4.

The distribution of $\Delta v$ is deduced from Equation (3) and the boundary condition $\Delta v = 0$ at $x_P = 0$:

$$\Delta v_P = \frac{6\Gamma}{c^4}\frac{\partial c}{\partial y}(x_P^3 - c x_P^2) + \frac{1}{c^3}\frac{\partial \Gamma}{\partial y}(3c x_P^2 - 2x_P^3) \tag{12}$$

All 3D simulations presented in this paper are performed using the above distributions of $\Delta u$ and $\Delta v$.

## 3. NUMERICAL IMPLEMENTATION OF THE AS MODEL

### *3.1. Presentation of the model*

To solve the set of partial differential equations describing the flow (the Navier–Stokes equations in their incompressible, inviscid, steady-state form), the 2D and 3D CVFEM of Masson *et al.* [16] and of Saabas [17] are used with appropriate modifications. These methods are typical, in their formulation, of modern commercial CFD software such as CFX Ansys and Fluent. In-house CVFEM codes are preferred here since the flexibility of commercial softwares is not sufficient to implement the proposed mathematical model. The 2D method is used to model problems like wings of infinite aspect ratio or actuator disks (the 2D method is able to model axisymmetric flows), whereas the 3D method is used for the analysis of rectangular ASs in translation or in rotation. For a better understanding of the AS implementation, a brief review of the 2D CVFEM follows using more or less the same notation as in Reference [16]. Owing to the extreme similarity between the 2D and 3D CVFEM algorithms and inner characteristics, the following is also applicable to the 3D CVFEM.

As displayed in Figure 5(a), in the 2D CVFEM, triangular elements are drawn between nodes (shown as bold crosses) to discretize a 2D domain that is the plane of a 2D Cartesian coordinate system $(x, y)$ along which flow velocity components are $(u, v)$, respectively. Inside every triangular element, segments are drawn that connect the center of gravity (shown as bold circles) to the middle of the triangle sides. These segments are in fact control surfaces (CS) across, which mass and momentum fluxes are evaluated. This is presented in Figure 5(b), which shows how three CSs are defined inside one of the elements surrounding the central node of Figure 5(a), highlighted by a gray-coloured dashed triangular frame. Only two out of these three CSs (CS1 and CS3) are attached to the CV surrounding the central node of Figure 5(a), highlighted as a shaded area. Every node has its own CV and, through application of mass and momentum conservation principles to



DOI: 10.1002/fld

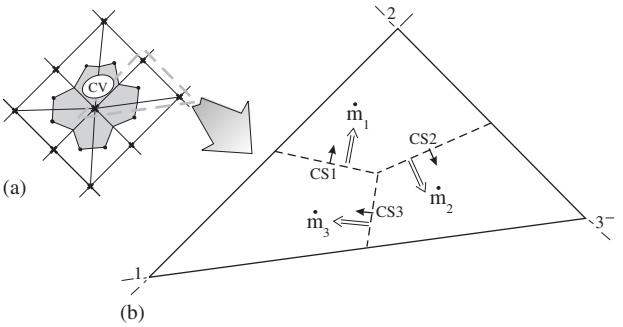


Figure 5. Details of the 2D CVFEM: element subdivision.

each one, the ultimate goal of the numerical method is to develop discretized equations of the general type

$$a_i^{\phi}\phi_i = \sum_{i,\mathrm{nb}} a_{i,\mathrm{nb}}^{\phi}\phi_{i,\mathrm{nb}} + b_i^{\phi} \tag{13}$$

where $\phi$ is used to represent either the components of velocity $(u, v)$ or the pressure $p$: $\phi = u$ or $v$ or $p$. $a^{\phi}$ and $b^{\phi}$ are discretization coefficients that establish the relative influence between the central node (numbered using the index $i$) and its neighbors (referred to as $i, nb$).

As regards pressure ($\phi = p$), discretized equations are built by applying mass conservation principles inside every CV. Mass fluxes occurring across the CSs of every finite triangular element are estimated from the integration of velocities across the CSs, but velocities are written as a combination of a pseudo-velocity and local pressure gradient (Rhie-Chow interpolation). More precisely, the velocity components used to derive mass fluxes are cast under the form

$$u^m = \hat{u} + d^u \left(-\frac{\partial p}{\partial x}\right)_{\mathrm{element}} \tag{14}$$

$$v^m = \hat{v} + d^v \left(-\frac{\partial p}{\partial y}\right)_{\mathrm{element}} \tag{15}$$

where $\hat{u}$ and $\hat{v}$ are the components of the pseudo-velocity field, $d^u$ and $d^v$ are the pressure coefficients and the subscript *element* is used to indicate that the pressure gradient is relative to the triangular element. For example, for the element shown in Figure 5(a), the contribution of mass fluxes to the global balance of the CV centered around node 1 is $\dot{m}_1 - \dot{m}_3$, where $\dot{m}_1$ and $\dot{m}_3$ are the mass fluxes across CS1 and CS3, respectively. Since the addition of all mass fluxes must be null for each CV in the solution domain, the algebraic decomposition of CS mass fluxes for every element, and then, their further assembly for each CV, yields a discretized set of equations relating pressures between nodes and their neighbors of the type described in Equation (13). In the algebraic decomposition process, pseudo-velocities and pressure coefficients, which are stored at the domain nodes, are linearly interpolated at the center of all CSs of a triangular element and are assumed to prevail over the CS, while discretization of pressure gradients is made assuming that pressure varies linearly over the triangular element.



DOI: 10.1002/fld

As regards momentum components (discussing only the case $\phi = u$), the balance made on each CV to express the $x$-component of Newton's law includes momentum fluxes through CSs, external and body force contributions and eventually diffusive contributions to represent the action of viscosity (or turbulence in RANS modeling). The $a_i^u$ and $a_{i,\mathrm{nb}}^u$ terms of Equation (13) arise from the algebraic decomposition of CS momentum and diffusive fluxes and their further assembly for the CV surrounding node $i$. Diffusive fluxes are accounted for by assuming a linear variation of the $u$ component within one element whereas momentum fluxes require the introduction of a convection scheme. Across one CS, the momentum flux is indeed calculated as $\dot{m}_j \times u_{\mathrm{CS}j}$ where $u_{\mathrm{CS}j}$ is the value of the convected variable across (and averaged over) CS $j$. The role of the convection scheme is to establish a relation of the type $u_{\mathrm{CS}j} = c_1 u_1 + c_2 u_2 + c_3 u_3$: in this work, the first-order and second-order mass-averaged-weighted (MAW) schemes developed, respectively, by Saabas [17] and Tran *et al.* [18] have been used. The $b_i^u$ term of Equation (13) comes from the contributions of pressure and the $x$-component of the external force acting on the CV. Pressure contributions are calculated again assuming a linear variation of pressure within every triangular element (and using Stokes' theorem inside the element).

The further split of the $b_i^u$ term shows how pseudo-velocities and pressure coefficients are evaluated by the CVFEM. To illustrate this, Equation (13) is recast under in the following form:

$$a_i^u u_i = \sum_{i,\mathrm{nb}} a_{i,\mathrm{nb}}^u u_{i,\mathrm{nb}} + \widetilde{b}_i^u + \mathbb{\nvDash}_{\mathrm{CV}} \left( -\frac{\partial p}{\partial x} \right)_{\mathrm{CV}} \tag{16}$$

where the $\widetilde{b}_i^u$ term is uniquely due to the contribution of external forces. Using Stokes' theorem, the pressure term distinctively appears as the product between the volume of the CV, $\mathbb{\nvDash}_{\mathrm{CV}}$ and a pressure gradient averaged over the CV. Contrary to Equations (14) and (15), the pressure gradient is averaged over the CV rather than over the element: this particularity provides a mechanism to avoid spurious oscillations in the CVFEM. When both sides of the last equation are divided to form an expression like Equation (14), it appears that:

$$\hat{u}_i = \frac{\sum_{i,\mathrm{nb}} a_{i,\mathrm{nb}}^u u_{i,\mathrm{nb}} + \widetilde{b}_i^u}{a_i^u} \quad \text{and} \quad d_i^u = \frac{\mathbb{\nvDash}_{\mathrm{CV}}}{a_i^u} \tag{17}$$

The solution algorithm prescribes the operations to be performed sequentially before the full set of discretized equations is ready to be solved algebraically. As in the original CVFEMs, the SIMPLE solution algorithm is employed and tridiagonal matrix-type algorithms are used to solve the discretized equations since structured meshes have been exclusively used in this work.

Boundary conditions are either of the Dirichlet (fixed values) or Neumann (see Reference [19] for a deeper explanation of outflow treatment) or periodic/anti-periodic type (in the case of the two-bladed wind turbine in uniform flow studied in Section 4.2.3). As regards the pressure equation, the algebraic system of discretized equations is indeterminate since two pressure fields differing by a constant are both valid flow solutions. To solve for this indetermination, the pressure can be prescribed at one node of the mesh. However, to ensure that the iterative process converges toward a stable pressure field, pressure values at the exit nodes can also be all set equal to a constant (providing the exit is far enough so that this approximation becomes true). In the case of rotating ASs, the simulations are performed in a rotating, non-inertial, frame of reference to solve for the steady flow where the oncoming flow is helicoidal (since it is the sum of a uniform axial inflow and a rotating one). Other adaptations have been necessary to handle the rotational component of velocity and are presented in Section 4.2.3.



DOI: 10.1002/fld

### *3.2. Implementation of the AS*

Properly handling the occurrence of velocity and pressure discontinuities and the associated system of external forces of an AS in any CFD method requires substantial adaptations to the underlying method. In the case of finite-volume methods, the following principles should be regarded as guidelines when building mass and momentum balances for CVs that are linked to an AS:

- The component of mass fluxes tangent to the AS must account for the discontinuities in velocity.
- The momentum balance must account for the contribution of the system of forces associated to the AS (presented in Equation (8)).
- The pressure contribution to momentum balance or to mass flux (when pressure gradients influence mass flux) must also account for the pressure jump. It is important to note that the contribution of the pressure jump, at the intersection between the AS and the CV, acts to cancel the contribution of the force component normal to the AS.

In the case of the collocated 2D CVFEM employed in this work (it is noteworthy that the following reasoning is readily applicable to the 3D CVFEM), it is more convenient to discretize an AS by placing nodes directly on its surface as illustrated by Figure 6(a), which shows an AS and the CV for one of the nodes located on the AS (the AS is depicted using a thick bold line). The CVs of the nodes that define the AS are not the only CVs of the solution domain where specific adaptations are required: all other CVs whose nodes are connected to at least one node of the AS need to be treated adequately. To perform these adaptations, it is essential to first orient the AS, i.e. to define on which side the discontinuities in velocities and pressure are to be applied, as already presented in Section 2.1. Triangular elements that form a part of CVs near the AS can then be classified depending on which side of the AS they rest: when an element is on the side where discontinuities must be applied, and has some connection to the AS nodes, it will be referred to as being part of the set of elements on the other side (SEOS). At the AS nodes, the values of the variables stored do not account for discontinuities: in a sense, AS nodes are not part of the SEOS even though they are infinitely close to it. But for triangular elements that are part of the SEOS, the values of the variables to consider when dealing with AS nodes must take into account the corresponding discontinuities appropriately. This is the underlying idea regarding the necessary adaptations summarized below:

- During evaluation or algebraic decomposition (when building the pressure or momentum equations) of mass or momentum fluxes, for all triangular elements that are part of the SEOS, if one or two of the three nodes defining the element is a node located on the AS:
  - Augment the values of $u, v, \hat{u}$ and $\hat{v}$ of the AS node(s) involved by $\Delta u, \Delta v, \Delta u$ and $\Delta v$, respectively, when evaluating or algebraically decomposing mass or momentum fluxes. Since the discontinuities are tangent to the AS, setting the discontinuities of pseudo-velocities equal to those of the velocities is correct from the point of view of mass conservation.
  - Augment the values of pressure at the AS node(s) involved by $\Delta p$ when evaluating or algebraically decomposing the pressure gradients of Equation (16) or of Equations (14) and (15).
  - Calculate the AS-attached external force contributions to CVs of AS nodes. Note that the component of the force normal to the AS cancels with the pressure discontinuity. Hence, when calculating the pressure contribution to a CV momentum balance, the specific



DOI: 10.1002/fld

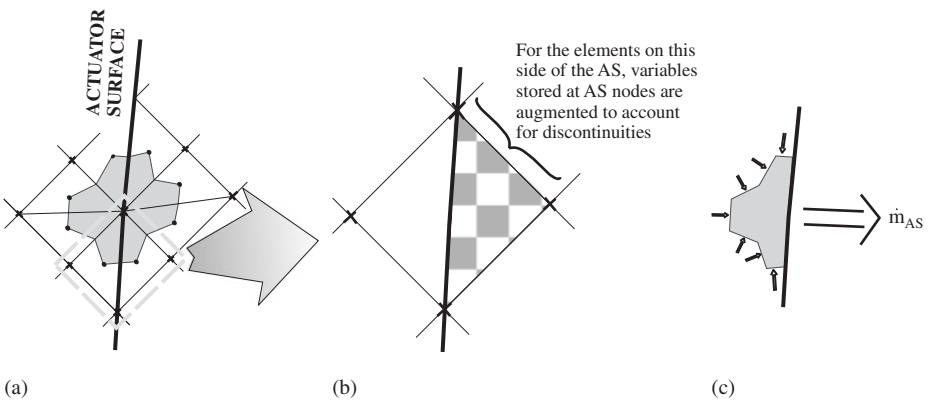


Figure 6. Details of the 2D CVFEM: treatment of the AS.

contribution due to the pressure jump cancels with the normal force contribution. The remaining pressure contributions are therefore calculated from the assembly of the pressure gradient volume integration within each element defining the CV. However, components of the force tangent to the AS need to be explicitly taken into account (the $f_x$ and $f_y$ expression of Equation (8)). Since these components are equal to the product of the local discontinuity in velocity and mass flux crossing the AS, to be consistent with the principles of the CVFEM, for a CV of an AS node, the mass flux crossing the AS is calculated as the sum of all mass fluxes crossing the CSs of the CV on one side of the AS only. Figure 6(c) provides an illustration of this calculation in the 2D method: $\dot{m}_{AS}$ corresponds to the mass flux crossing the AS and is equal to the sum of all mass fluxes crossing the CSs on the left side of the AS. The mass fluxes through CSs are those used during the construction of the algebraic equations expressing mass balances, since mass conservation is guaranteed by the CVFEM, the choice of side where the sum of mass fluxes is calculated has no consequence on the converged solution.

### *3.3. Overall solution algorithm*

When the loading of the AS is prescribed and is independent of the flow, a unique flow solution exists that respects the principles of mass, momentum and vorticity conservation. In the numerical solution of this problem, the adapted CVFEM simply converges toward a single flow solution, as would the CVFEM also converge if a prescribed set of volume forces were used instead to model a lifting body. However, when the loading of the AS is dependent on the flow, an iterative process must take place:

1. Initialization of the flow solution (generally to uniform inflow).
2. Estimation of AS(s) loading: in the case where lifting devices are modeled, this consists of evaluating relative flow angles and velocities at control points (to be defined in Section 4) and, from considerations of airfoil aerodynamic characteristics, estimate the distribution of circulation at every section of the AS. Once circulation is known, the action of the AS is modeled using the distributions of Equations (11) and (12) for velocity discontinuities and Equation (8) for external forces.



DOI: 10.1002/fld

3. Application of adapted CVFEM to find the flow solution given loading defined in Step 2.
4. Re-estimation of the AS loading: an iterative process takes place between Steps 2 and 3 until convergence of the flow solution.

In Step 3, it should be kept in mind that the CVFEM is also undertaking an iterative process to find a fully converged flow solution. But, it is not always necessary to use the converged solution before re-evaluating the AS loading, thereby accelerating the global convergence of the four-step process. To ensure a smooth convergence process, the AS action on the flow can also be introduced gradually. For the particular problem of the uniformly loaded actuator disk, this approach proved to be essential.

## 4. RESULTS

The concept of the AS is first applied to simple 2D problems having analytical solutions and for which the distribution of discontinuity is given: excellent agreement with flow properties and force evaluation is found. The method is then applied to the 3D problem of the tapered wing in translation and is compared with the results of the Prandtl lifting line. Finally, the method is applied to wind turbine aerodynamics by using rotating ASs.

### *4.1. 2D problems*

*4.1.1. The segment with uniform velocity discontinuity.* The first validation of the proposed approach concerns the simple case of a 2D segment along which a uniform velocity discontinuity is applied in the segment direction. This 2D segment is immersed in a uniform flow, therefore the exact analytical solution is the combination of the uniform flow (of magnitude $U_\infty$) plus the perturbed flow due to the velocity discontinuity, which can be attributed to a vorticity distribution, according to the Biot–Savart Law. The solution domain is a rectangle oriented in the direction of $U_\infty$, and the value of the uniform velocity is prescribed on three faces of the domain, while the last face is defined as an outlet boundary. Figure 7 presents the streamlines of the numerical solution as well as isocontours of the vertical velocity component for the case of a segment-oriented parallel to the uniform inflow. Figure 8 presents the same results, but for the perturbed solution only, i.e. for the flow induced by the vorticity distribution. This flow is deduced from the numerical solution by subtracting the value of $U_\infty$ from the computed velocity field. In all figures, the AS is drawn using a bold dashed line. In Figure 8, the left side shows the solution obtained using a coarse grid of approximately 2500 nodes whereas the right side shows the solution obtained using the same domain dimensions but for a much finer grid of over 400 000 nodes (for clarity, only one mesh point over 4 is shown in the drawing). In the case of the coarse mesh, the streamlines of the numerical solution are not perfectly circling the segment of discontinuity as they theoretically should, based on the analytical solution. In the case of the fine mesh; however, the streamlines shape is very close to perfect circles, although some irregularities can still be observed. In fact, it has been verified that the mesh resolution guaranteeing grid independence for the problem of the segment with uniform velocity discontinuity has to be much finer than the mesh resolution that would guarantee grid independence when studying the segment with a parabolic distribution. The uniform distribution is a more difficult distribution to study with the CFD method because of the sharp discontinuity it induces at the edges of the segment.



DOI: 10.1002/fld

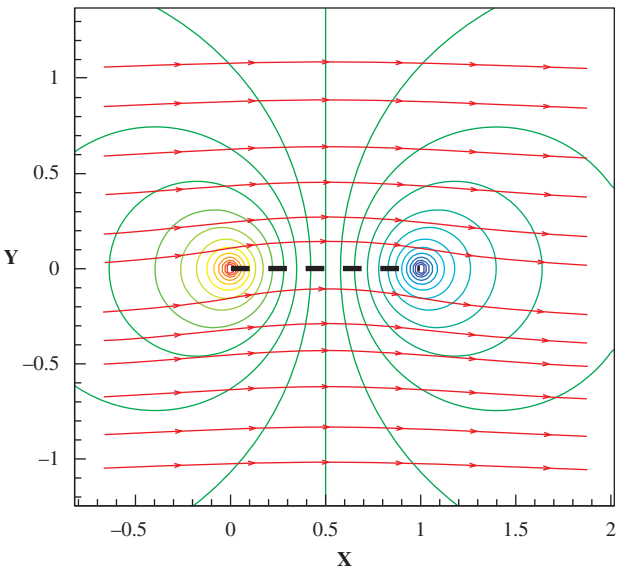


Figure 7. Streamlines and isocontours of vertical velocity for the 2D segment.

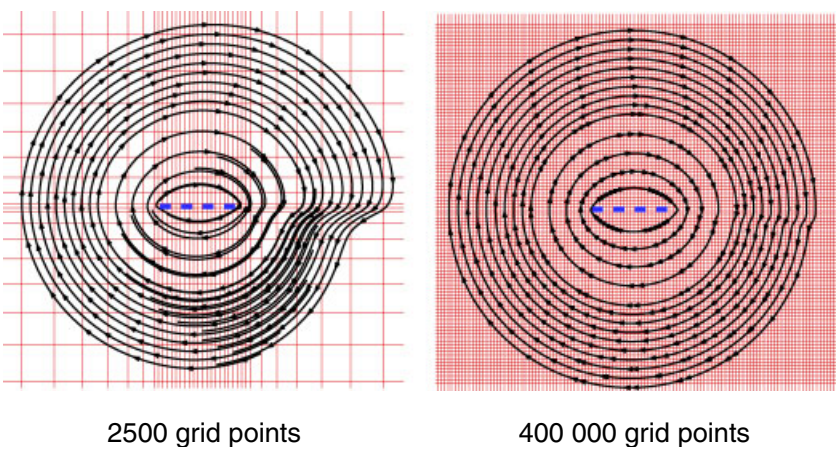


Figure 8. Streamlines of the perturbation flow as a function of spatial discretization.

To evaluate the impact of the uniform inflow on the perturbed solution, numerical computations have been performed for incoming flow angles of 0, 10, 30, 60 and 90° with respect to the segment representing the AS and for different ratios between $U_\infty$ and attached vorticity (see Figure 9 for an illustration of the different configurations studied). For all solutions, the total external force that the vorticity segment induces on the flow has been calculated. It has been verified for all cases that the integrated component of the force in the direction of the incoming free velocity is always very close to zero (to within a few percent of the lift), while the integrated normal component



DOI: 10.1002/fld

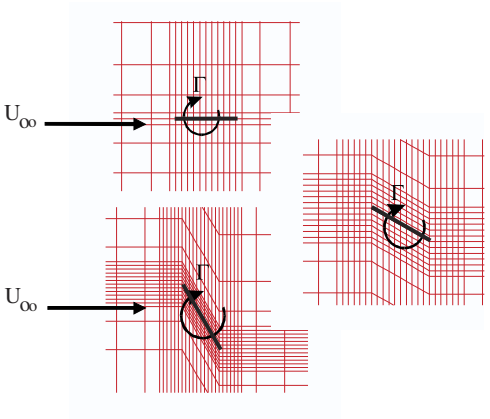


Figure 9. Different configurations for the 2D segment.

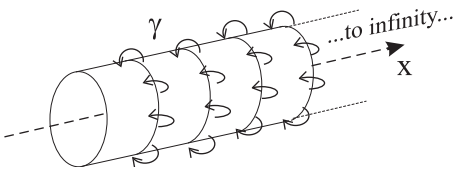


Figure 10. The ring vortices system of a uniformly loaded actuator disk.

of the force is always very close (within 4%) to the Kutta–Joukowski relation, which states that induced lift is equal to $\rho U_\infty \Gamma$ (where $\Gamma$ is the total circulation $\Gamma = c\Delta u$, $c$ being the length of the vorticity segment).

*4.1.2. The actuator disk.* As regards the well-known actuator disk problem, it is possible to distinguish two vortex systems that induce perturbations in the incoming flow: the first vortex system consists of a hub vortex of constant strength together with radial vorticity distributed on the actuator disk and axial vorticity on the slipstream surface. The slipstream surface should be geometrically defined by the trajectories of the particles passing through the actuator disk contour. Determining these trajectories is not a trivial problem [20] and for the sake of simplicity, the geometry is taken as a line extending from the actuator disk contour to downstream infinity. This first vortex system conserves vorticity flux and induces only azimuthal velocities in the flow. The second system consists of ring vortices distributed over a contracting tube shed from the edge of the actuator disk and extending to downstream infinity (see Figure 10). This system induces radial and axial components of the perturbation velocities, and it is also responsible for slipstream contraction.

The present method, in its axisymmetric version, has been used to simulate the action of the second system by studying a constant surface distribution of velocity discontinuity of magnitude $\gamma$ for the ring vortices. These conditions correspond to those of a uniformly loaded actuator disk.



DOI: 10.1002/fld

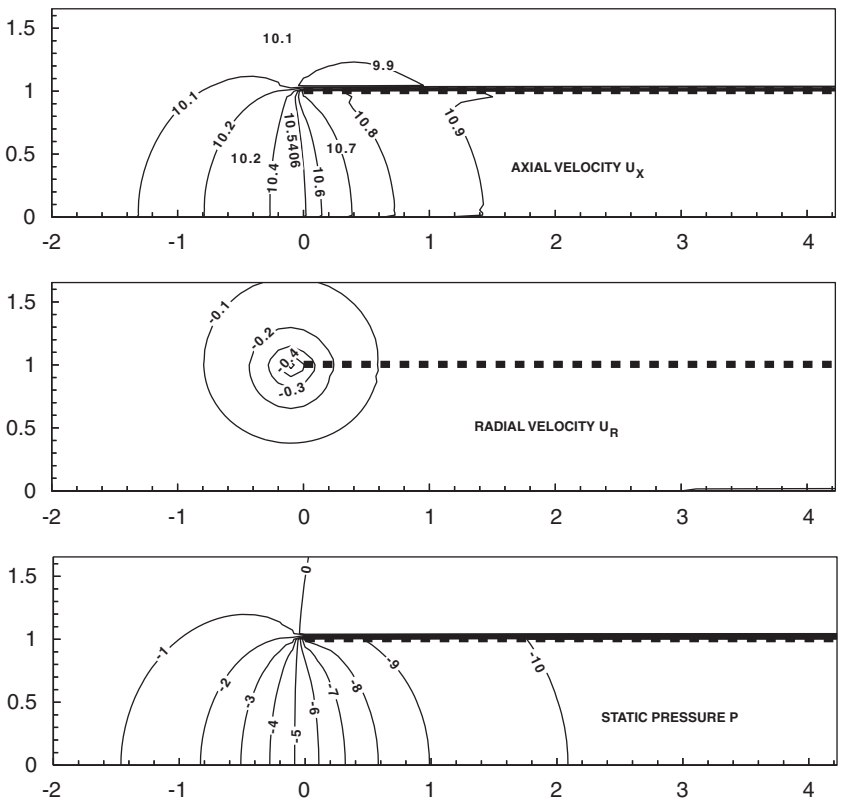


Figure 11. Solution properties for the case of the uniformly loaded actuator disk.

The full analytical solution to this problem can be found in the literature [21]; among various results, the variation of the perturbation axial velocity at the axis of symmetry is given by

$$u_x(r=0,x)=\frac{\gamma}{2}\left(1+\frac{x}{\sqrt{R^2+x^2}}\right)$$

where $R$ is the radius of the actuator disk located at $x=0$ and $u_x$ is the axial velocity. The computations have been done with a uniform inflow velocity of 10 m/s, a 1 m radius actuator disk and a velocity discontinuity $\gamma$ of 1 m/s. Some convergence issues were encountered, mostly due to instabilities developing at the outflow boundary (the AS used here indeed extends up to the outflow boundary). Building successive solutions to the problem by stepwise increasing the AS solves this problem and ensures rapid convergence. Figure 11 presents isocontours for the axial and radial velocities $u_x$ and $u_r$, as well as the static pressure $p$. In this figure, the AS is represented by a bold dashed line; note that the tangential component is null since only the second vortex system of the actuator disk is studied.

Figure 12 presents a comparison between numerical and analytical solutions of the centerline velocity variation. The agreement is very good.



DOI: 10.1002/fld

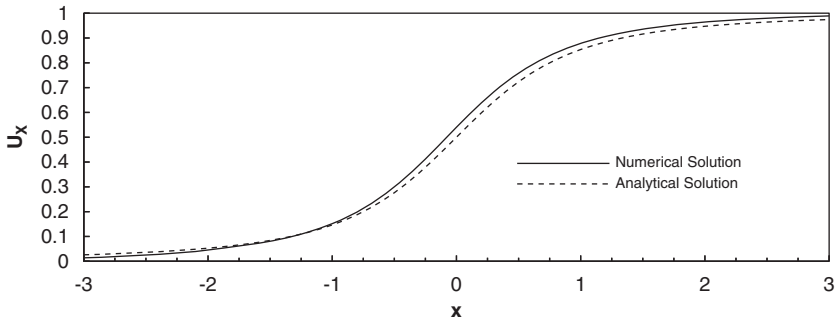


Figure 12. Centerline velocity variation.

*4.1.3. Axisymmetric actuator disk applied to horizontal-axis wind turbines (HAWTs).* The embedding of an actuator disk within a CFD method is an area of increasing interest in the field of horizontal-axis wind turbine (HAWT) aerodynamics [22] and the proposed CVFEM has been applied using the axisymmetric actuator disk concept [23] and blade-element theory. Whereas the present formulation uses surface forces, almost all other models represent the actuator disk by a set of volume forces only [24–26]. In Reference [23], the results produced by the proposed AS method have also been compared with the results of a previous method, developed by the same authors, in which the velocity field is not allowed to be discontinuous and the actuator disk is analyzed as a source of external force only (resulting in fact in a pressure jump) to mimic the behavior of volume force methods. As observed by some authors [25, 26], spurious oscillations (of a checkerboard type) in flow properties occur in the vicinity of the actuator disk when the flow is assumed continuous; however, using the representation of the AS as presented in this article, such anomalies are not observed. Furthermore, the relative differences in predicted mechanical power output between the two methods have been evaluated to be 5% on average (based on studies of four wind turbines).

### *4.2. 3D problems*

*4.2.1. The finite wing.* The problem of the finite wing in uniform translation is a necessary step to verify the proposed method's capability to model wake induction on a lifting device. If the method performs adequately for a wing in translation, then it is expected to perform well for a wing in rotation.

Twenty-four forms of the tapered wing have been studied derived from the combinations of 6 taper ratios $c_t/c_r$ (0.1;0.2;0.4;0.6;0.8;1.0) and 4 aspect ratios AR$(4; 6; 8; 10)$. The same span length $b$ of 10 m, inflow velocity of 50 m/s and pitch angle $\beta$ of 5° have been set for all the 24 cases. AR is defined as the ratio of $b^2$ to the wing area.

The AS used to model the finite wing is a flat tapered plate parallel to the incoming flow (of velocity $U_\infty$ along the $x$ direction), whose dimensions are those of the wing planform shown in Figure 4. The solution domain is a cube with sides of length $30b$; the flat plate representing the wing is located $10b$ downstream of the inlet and at the center of $(y, z)$ planes. The mesh is refined in the vicinities of the wing tips and around the leading and trailing edges, and nodes are placed at mid-chord of the wing as control points where the induced angle $\alpha_i$, evaluated using $\alpha_i = \tan^{-1}(-w_{\text{av}}/U_\infty)$, is measured (see Figure 13 for an illustration of mesh details around



DOI: 10.1002/fld

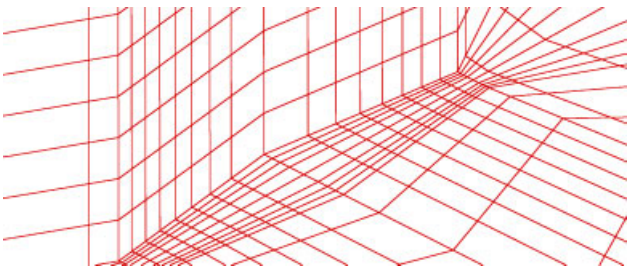

Figure 13. Mesh details around the actuator surface.

Table I. Meshes and needed RAM.

| | Mesh **M1** | Mesh **M2** | Mesh **M3** |
|---|---|---|---|
| Number of nodes for domain discretization | $41\times31\times49$ | $81\times61\times97$ | $161\times161\times193$ |
| Number of nodes for wing discretization | $6\times16$ | $12\times32$ | $24\times64$ |
| RAM needed (approximately) | 100 Mb | 800 Mb | 6.4 Gb |

the AS). To estimate the loading of the AS, the lift coefficient is calculated using the thin airfoil relation $C_l = 2\pi(\beta - \alpha_i)$, so that the circulation around a section is given by $\Gamma = \pi c U_\infty(\beta - \alpha_i)$. Velocity discontinuities are distributed using Equations (11) and (12) and the associated system of forces using Equation (8).

Table I summarizes the characteristics of the three meshes used to discretize the solutiion domain along with the total RAM needed to analyze the problem. Since mesh M3 requires a substantial amount of computational power, few computations are performed using this mesh.

Total lift $L$ of the wing is calculated from the surface integral of pressure jumps across the AS while induced drag $D_i$, which is equal to the in-plane load that results from the crossflow experienced by the AS, is determined from momentum consideration using:

$$D_i = -\int\int_S \rho \Delta u w_{\text{av}} \, \mathrm{d}S \tag{18}$$

In these equations, $\rho w_{\text{av}} \, \mathrm{d}S$ corresponds to the mass flux passing through an elementary surface of area $\mathrm{d}S$, and is in fact evaluated from the assembly of mass fluxes across all CS on one side of a CV as discussed in Section 3.2.

Figure 14 presents (a) a downstream view of streamlines concentrated at the tips of a wing of AR = 10 and taper ratio of 1, and (b) the same view, but with a slight inclination of the $x$ axis to present downstream development of tip vortices. In the exact, analytic solution to this problem [20], the downstream vorticity system exhibits a natural tendency to roll up in singular, hardly predictable, behavior. To use vortex methods to analyze the aerodynamics of a lifting device, it is necessary to rely on a specific model for the trailed vorticity system usually by setting, in advance, the shape of this system. The shape can be set fixed or moving with the flow. When set moving, singular behaviors are noted and the problem becomes less tractable. Figure 14 indicates that vorticity creation and advection is well modeled by the present method: $\Delta u$ and $\Delta v$ discontinuities result in the creation of vorticity within the flow (with a major component along the $x$ axis), whose evolution is naturally taken into account by the Navier–Stokes equations.



DOI: 10.1002/fld

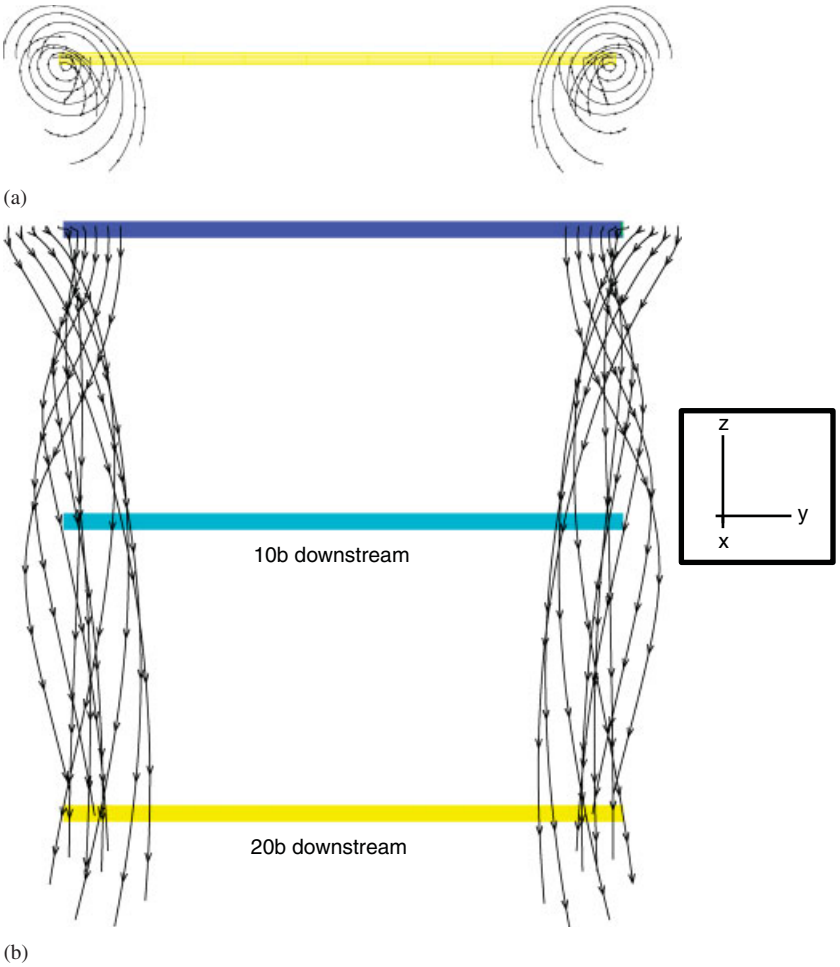


Figure 14. Highlighting tip vortices: flow streamlines.

In the actual, viscous flow of a finite wing, boundary layers occur along the wing surface but, for large Reynolds number, they are very thin and outside them the flow acts according to inviscid flow theory. At the trailing edge of the wing, these viscous layers continue to exist in the wake and viscosity effects act to rapidly equalize the values of velocity and pressures across the wake. In the AS, the component of lateral velocity discontinuity cancels abruptly at the trailing edge, however, the method reproduces with good accuracy the results of the Prandtl lifting line theory.

To present the influence of the convection scheme order, isocontours of the calculated component $w_{av}$ of the flow crossing the AS are drawn in Figure 15 for a wing of AR$=4$ and taper ratio of 1, using either the first- or the second-order convection scheme with mesh M2. Along the entire wing span, the flow component $w_{av}$ is observed to decrease from positive (upwash) to negative (downwash) in accordance with analytical vortex analysis. Intense lateral variations of $w_{av}$ happen at the tip where the influence of tip vortex induction on the flow is the strongest. This



DOI: 10.1002/fld

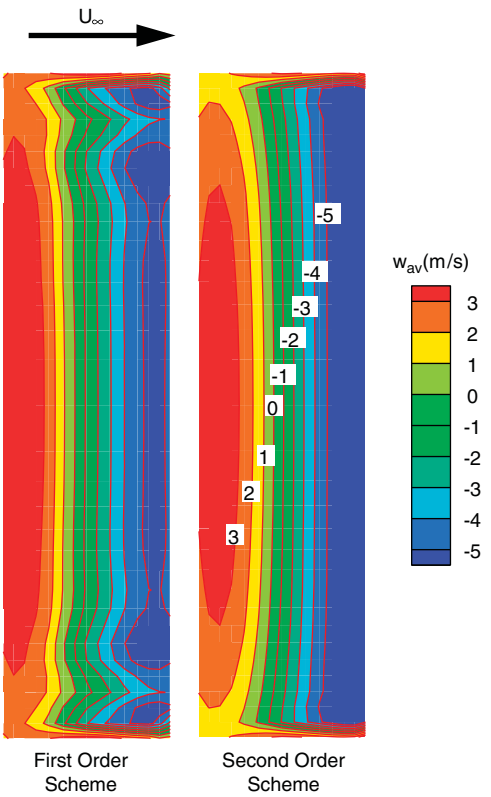


Figure 15. Convection scheme effect on crossflow isocontours.

behavior, linked with the fact that lift should cancel at the tip, is difficult to handle numerically. The second-order convection scheme notably improves modeling of the tip area. As underlined by Tran *et al.* [18], the second-order scheme is more efficient in modeling regions of rapid velocity variation. Reduction of false diffusion is also evident with the second-order scheme, since the axial decrease in $w_{\mathrm{av}}$ component is less intense than with the first-order convection scheme.

Figure 16 shows the induced flow angle in the plane defined by the wing surface at two stations along the flow direction: mid-chord and $0.8c_r$ ($c_r$ is the root chord length) upstream of the leading edge. At the mid-chord position, the induced flow angle is simply the opposite of the induced angle $\alpha_i$. Results for the three meshes and two convection schemes are presented. Results at mid-chord were also produced using Prandtl lifting line theory with the method described by Anderson [27] using 200 points to discretize the wing planform. The differences in induced flow angle predictions between convection schemes are significant at mid-chord, but much less so at the 80% upstream position. Furthermore, improvements in the mesh refinement do not seem to diminish these differences at the 80% upstream position. These observations lead to a preliminary conclusion that regardless of the convection scheme or mesh, using the upstream inflow angle (and a suitable relation between this angle and the effective angle of attack of the airfoil $\beta-\alpha_i$) instead of the effective flow angle is a better choice for estimating the loading of a wing. Finally, it should



DOI: 10.1002/fld

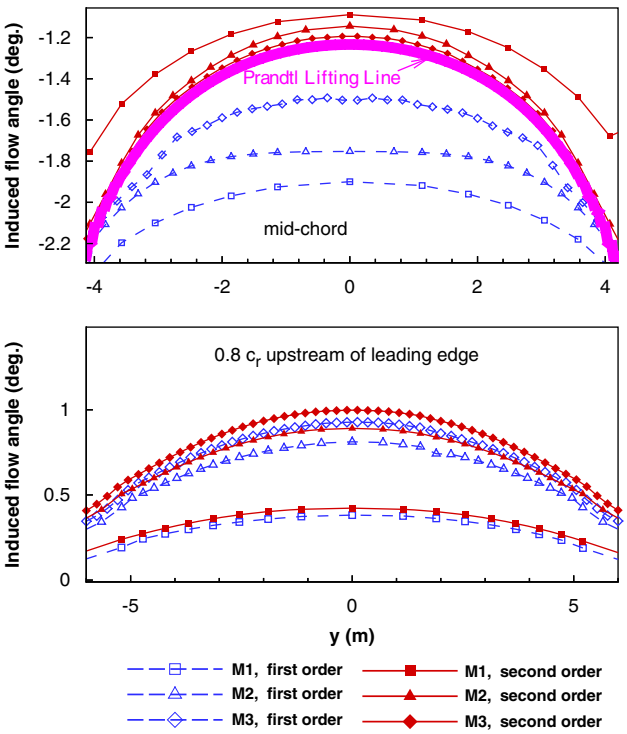


Figure 16. Spanwise distributions of induced flow angles at single layer of control volumes.

be noted that an excellent agreement exists between results of Prandtl lifting line theory and the results from the new method with second-order scheme and meshes M2 and M3: both approaches are therefore equivalent in the treatment of the vortical wake of a finite wing.

Finally, the proposed method is used, with the second-order convection scheme, to predict values of lift $L$ and induced drag $D_i$ for all 24 planforms studied. Using the Prandtl lifting line adaptation of Anderson as a reference, the performance of the method is measured by calculating the relative differences for lift $|L-L_{\text{Prandtl}}|/L_{\text{Prandtl}}$ and induced drag $|D_i-D_{i,\text{Prandtl}}|/D_{i,\text{Prandtl}}$ and reported in Figure 17 as a function of taper and aspect ratio. Results obtained from a modified version of the proposed method are shown as well: in this formulation, velocity discontinuities are not allowed at the AS (the velocity field is continuous) but the system of forces is still prescribed using the equations of the original method. In some way, the modified method is trying to emulate a volume force approach where the forces would be distributed over a mid-chord and $0.8c_r$ upstream. In a CFD adaptation of the volume force approach for the finite-wing problem, prescribing the forces from flow properties is not obvious; the origin of the induced drag and its evaluation is not straightforward either. The AS however represents an integrated framework that performs this task with accuracy when compared with the results of the Prandtl lifting line adaptation of Anderson. Indeed, Figure 17 shows that the relative performance of the proposed method for lift and induced drag ranges between 5 and 10% for meshes M2 and M3, whereas much higher relative differences are measured using the volume force approach. The ability of both methods to predict the ideal value of induced drag



DOI: 10.1002/fld

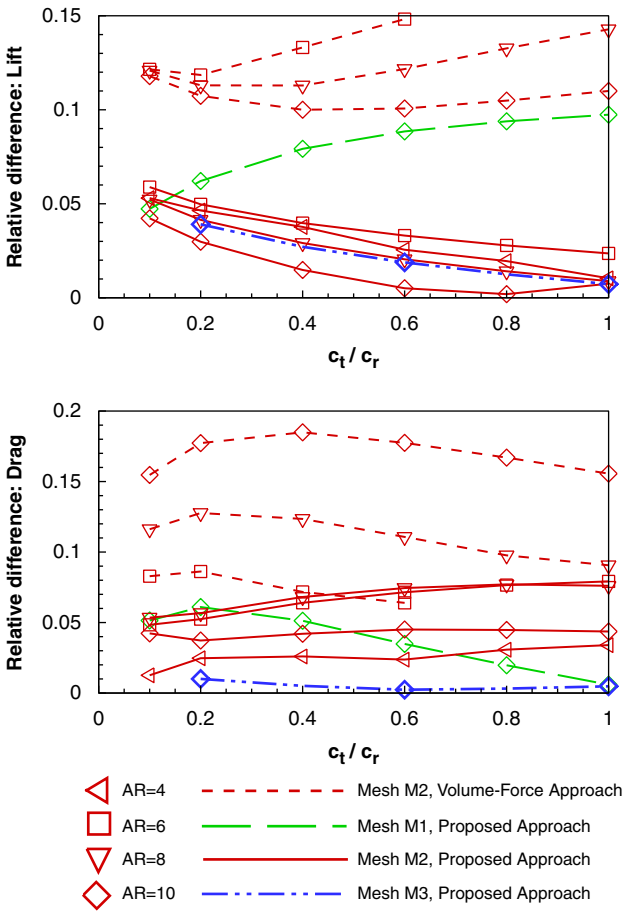


Figure 17. Relative performance of the method compared with the Prandtl lifting line.

(for a given lift) decreases when either AR or $c_r/c_t$ increases and is dramatically improved by the mesh refinement as shown by the results using mesh M3. As a rule of thumb, grid dependency has been studied and shows that a minimum number of 1000 nodes on the surface carrying discontinuities are needed for a wing planform of aspect ratio greater than 8 to give relative differences of lift and drag close to 2% when compared with the Prandtl solution.

*4.2.2. Vorticity conservation considerations.* Since vorticity is not explicitly represented in the wake (as it would be using vortex models), but is rather intrinsically handled by the CFD method, it is interesting to verify how it is conserved in the wake of the AS. As presented in Figure 18 for the finite-wing case, the proposed verification consists in examining vorticity fluxes, or from Stokes' theorem, circulation characteristics in the wake. Let us define :

$$\Gamma_W(x, y) = -\int_{-\infty}^{+\infty} w(x, y, z)\, \mathrm{d}z \tag{19}$$



DOI: 10.1002/fld

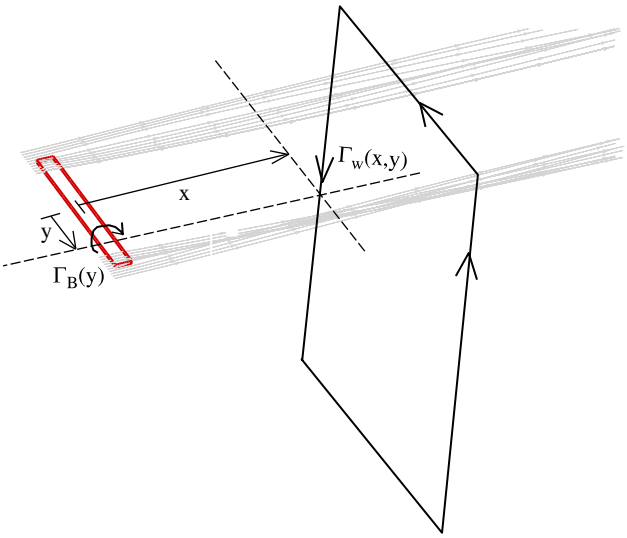


Figure 18. Illustrating vorticity flux conservation in the wake of a finite wing.

Then, it is expected that $\Gamma_W(x, y) \approx \Gamma_B(y)$ where $\Gamma_B$ is the bound vorticity of a wing section at the spanwise location $y$ ($y=0$ being at mid-span). This equality is only approximate since wake expansion occurs, hence with increasing $x$, it is expected to become less valid. This is verified in Figure 19 where it is visible that in the near wake, distribution of circulation closely matches the bound vorticity distribution, whereas further downstream the distributions are smeared out due to numerical and viscous diffusion. However, the circulation is not found to reach zero for spanwise positions $y > b/2$, as it should be. We believe that this undesired behavior is due to the finiteness of the domain (the integral of Equation (19) is limited by the domain extents) and to the choice of boundary conditions on the side of the calculation domain where velocities are imposed to be equal to the incoming velocity $U_\infty$, which prevent the perturbations induced by the wing vortices system to be represented on the domain sides.

*4.2.3. The wind turbine.* In this section, rotating ASs are employed to study HAWT aerodynamics. Loading of the AS is prescribed in the same way as for the finite wing. The CVFEM, however, had to be adapted to the resolution of Navier–Stokes equations in a rotating frame of reference: this issue is discussed first, and results for a small, experimental wind turbine are then presented.

*4.2.3.1. Numerical implementation of the wind turbine model. Reformulation of the mathematical problem.* The rotating frame of reference, in which the blades appear fixed, has been used for simulations. In this reference frame, the governing equations are the Navier–Stokes equations in their steady form including inertial (centrifugal and Coriolis) forces. When pressure and flow velocity components (measured in a Cartesian coordinate system) are selected as the unknowns to this problem, and the CVFEM formulation of Saabas [17] is used to discretize the algebraic equations for these unknowns, numerous convergence problems arise, even for the simple case of an advancing flow in solid rotation without obstacle (corresponding to the inlet condition of the wind turbine problem). Investigations have determined that the convection scheme, in combination



DOI: 10.1002/fld

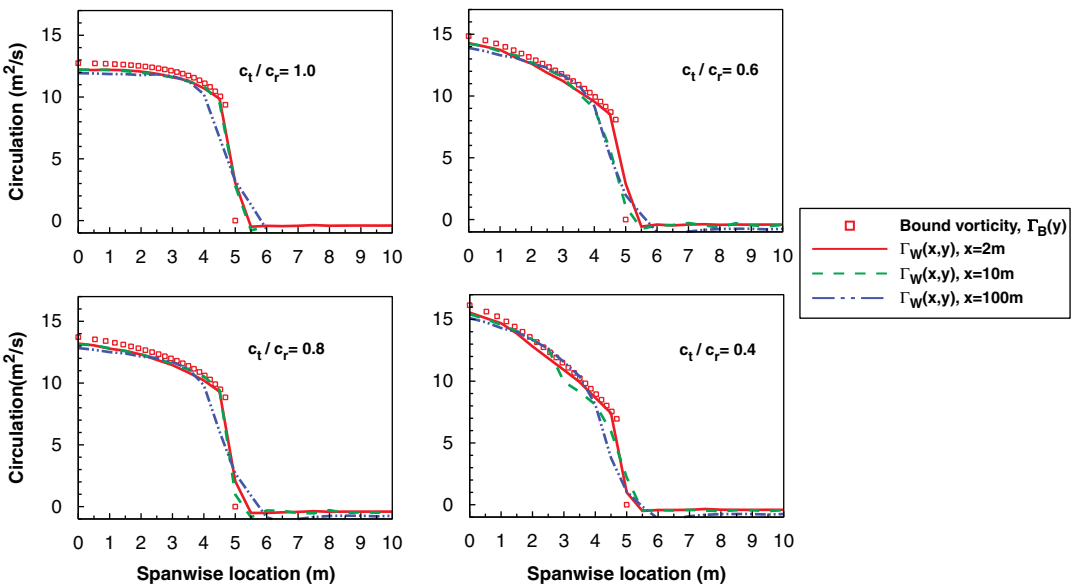


Figure 19. Comparison between bound and wake vorticity.

with the segregate solution algorithm, is inappropriate to adequately handle the convection fluxes specifically due to the rotating component of the velocity $\Omega r$ ($\Omega$ is the blade rotational speed and $r$ is the distance to the axis of rotation). To resolve this convergence problem, the flow velocity $\mathbf{V}$ as measured in the rotating frame of reference is split in two parts

$$\mathbf{V} = \mathbf{V}_{nr} - \Omega r \mathbf{e}_\theta \tag{20}$$

where $\mathbf{V}_{nr}$ is the velocity vector measuring the flow velocity in a fixed system of coordinates (see Figure 20) and $-\Omega r \mathbf{e}_\theta$ is the rotational velocity vector. The velocities $\mathbf{V}_{nr}$ at every domain node constitute the new unknowns of this problem. This separation of the velocity in two terms is introduced in the Navier–Stokes equations

$$\iint_S \rho \mathbf{V}(\mathbf{V}\cdot\mathbf{n})\,\mathrm{d}S = \iint_S p\mathbf{n}\,\mathrm{d}S + \iiint_V \rho\Omega^2 r\mathbf{e}_r - 2\rho\boldsymbol{\Omega}\times\mathbf{V}\,\mathrm{d}V \tag{21}$$

where the surface integrals are taken upon a CV $V$ of surface $S$ with $\mathbf{n}$ as the outward normal vector to the surface. The last two terms are inertial forces (centrifugal and Coriolis forces) due to the rotation of the reference system.

Following Equations (20) and (21), the convection term is split into three terms:

$$\iint_S \rho \mathbf{V}(\mathbf{V}\cdot\mathbf{n})\,\mathrm{d}S = \iint_S \rho \mathbf{V}_{nr}(\mathbf{V}\cdot\mathbf{n})\,\mathrm{d}S - \iint_S \rho\Omega r\mathbf{e}_\theta(\mathbf{V}_{nr}\cdot\mathbf{n})\,\mathrm{d}S + \iint_S \rho\Omega^2 r^2\mathbf{e}_\theta(\mathbf{e}_\theta\cdot\mathbf{n})\,\mathrm{d}S \tag{22}$$

On the right-hand side of Equation (22), the first term can readily be used to model the contribution of convection to the discretized momentum conservation equation using $\mathbf{V}_{nr}$ nodal values as unknowns, following the MAW scheme of Saabas [17] or the second-order scheme of Tran *et al.* [18].



DOI: 10.1002/fld

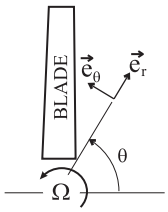


Figure 20. Parameters for wind turbine study; the arrow around Ω indicates blade direction of rotation (observer is upstream the blade).

The second and third terms on the right-hand side of Equation (22) are treated as constant source terms in the numerical model when building the algebraic equations from momentum conservation in a CV. The surface integral of the second term is calculated at Gaussian points on the surface and mass fluxes are evaluated again using the MAW scheme.

It can be shown that the third term on the right-hand side of Equation (22), combined with the inertial forces, will result in a total volume force given by $-2\rho\mathbf{\Omega}\times\mathbf{V}_{nr}$, where $\mathbf{\Omega}$ corresponds to the rotation vector (with direction along the axis of rotation). This volume force is, in some way, a Coriolis force that is applied only on the non-rotating component of the velocity.

This reformulation of the governing equation has proven to be very efficient and has been thoroughly tested on the case of an advancing flow in solid rotation without obstacle. Different boundary and initial conditions have been used on this case and, in almost every simulation, the solution rapidly converges toward the trivial solution $\mathbf{V}_{nr}=0$.

*Solution domain specifics:* Taking advantage of the symmetry of the two-bladed wind turbine problem, the solution domain is a hollow half cylinder as shown in Figure 21 with only one actuator surface used to model the rotor. Depending on the flow variable solved, periodic or anti-periodic boundary conditions are set at the surface of symmetry. As shown in the zoom of Figure 21, the structured mesh is composed of radial lines extending from an inner radial position (set small compared to the blade dimensions) to an outer position far from the blade. Let $I$, $J$ and $K$ be the indices for nodes of the structured mesh, then the previously mentioned radial lines correspond to $J=$constant, and providing that $u$, $v$ and $w$ are the flow components in the $x$, $y$ and $z$ axis as shown in Figure 21, then periodicity is expected for $u$ and anti-periodicity for $v$ and $w$ components between surfaces $J=1$ and $J=NJ$ as summarized by the formulas in Figure 21.

*Results for the TUDelft rotor:* In this article, the aerodynamics of an experimental rotor designed at Delft Technical University (TUDelft) is thoroughly studied. The TUDelft rotor is a two-bladed HAWT having a diameter $D$ of 1.2 m that rotates (for the cases studied in the article) at 700 rpm. An NACA0012 profile is used on the lifting part of the blade from $r/R=0.3$ to the tip, and the blade has a constant chord length of 0.08 m with a linear twist distribution. The blade can be pitched at different angles; herein, blade tip pitch angles of 0, 2 and 5° are used. Detailed inflow and near-wake measurements have been performed using hot-film anemometry. Information regarding the wind turbine and the research program of TUDelft can be found in the works of Sant [28] and Haans *et al.* [29].

Given the results of the finite-wing study, a structured mesh of $201\times65\times46$ nodes is used along axial ($I$), azimuthal ($J$) and radial ($K$) directions to discretize the domain of total length $3.5D$, inner radius $1.5\,10^{-2}\,D$ and outer radius $5D$. The mesh is refined around the AS location, which is located $0.3D$ upstream of the outflow boundary. As shown in Figure 22, which presents the



DOI: 10.1002/fld

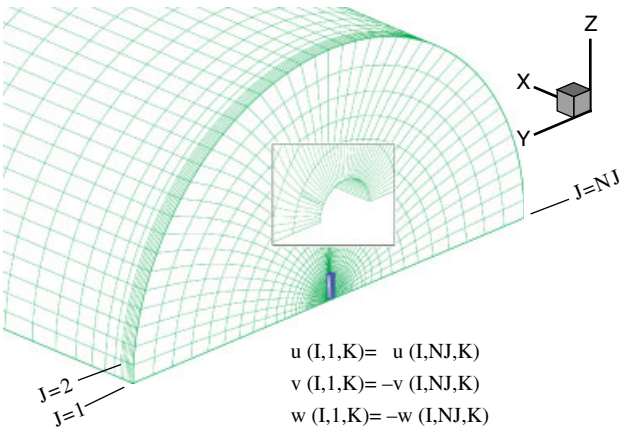


Figure 21. Mesh details for the wind turbine case.

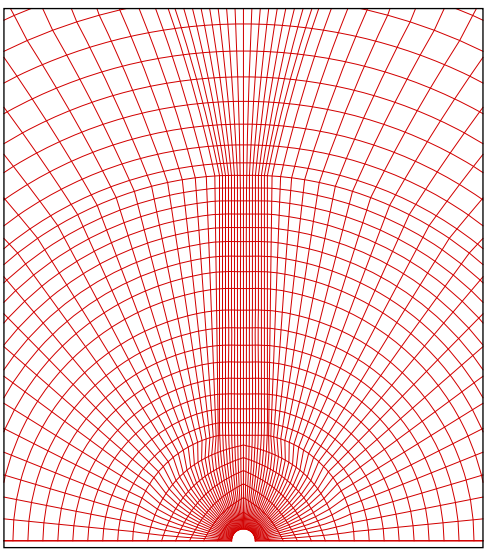

Figure 22. Axial mesh plane at actuator surface.

node distribution in the $I =$ constant plane where the AS lies, $17 \times 20$ nodes are used to discretize the AS.

The location of inflow and outflow boundaries relative to the AS has been studied to ensure the independence of results, together with the influence of the spacing between axial mesh planes in the vicinity of the AS. The final mesh design represents, in terms of total number of nodes, a good compromise between accuracy (in terms of grid independence) and computing time.

As regards AS loading, circulation around blade sections is calculated using relative velocities and angles of attack evaluated at the mid-chord of the blade to provide values of $\|\mathbf{V}_{av}\|$ and



DOI: 10.1002/fld

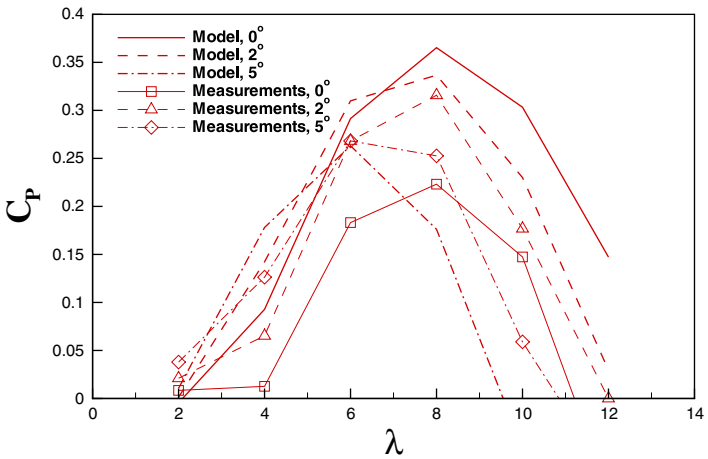


Figure 23. Power coefficient as a function of tip-speed ratio.

$C_l$ in Equation (10). During meshing, nodes are located in the middle of the blade, as illustrated by Figure 22, where a vertical line of nodes splits the AS into two equal parts. This practice is comparable with vortex methods based on the lifting line concept, where the blade bound circulation is estimated from values of velocities at control points [3].

2D experimental lift and drag coefficients are taken from [30] for a Reynolds number of 150 000. As explained in the presentation of the AS, only lift characteristics are needed to prescribe its loading. For all computations, the second-order convection scheme was used and an artificial viscosity was employed to ensure stability during the convergence process; it was verified that the level used did not influence the rotor inflow and near-wake results so that the following results reproduce inviscid flow.

*Power and thrust curves:* Figures 23 and 24 present comparisons between experimental and computed power and thrust coefficients as a function of tip-speed ratio $\lambda$ for tip-pitch angles of 0, 2 and 5°.

Power is calculated from blade-element theory using the local flow velocity calculated by the CVFEM (evaluated at the middle of the AS) and 2D lift and drag characteristics. Thrust is calculated from the surface integration of pressure discontinuities over the AS. The agreement with the experiment is much better for the thrust than for the power coefficient. The calculated power coefficient values are close to the experiment only for the 2° tip-pitch angle case.

$\lambda = \mathbf{8}$ *case: components of velocity:* To give some insight into the model results, Figures 25 and 26 present the velocity components (in m/s) calculated by the model for $\lambda = 8$, corresponding to a uniform incoming velocity of 5.5 m/s with the rotor rotating at 700 rpm. The pitch angle is 2°. The two figures show isocontours of the axial and radial (as defined by the system of coordinates of Figure 20) velocity components of $\mathbf{V}_{nr}$ taken either in the plane enclosing the rotor swept surface (Figure 25) or in the axial plane that splits the blade into two halves, i.e. $\theta = \pi/2$ (Figure 26). In Figure 26, the location of the AS is indicated by a straight bold line. Since only the non-rotating components of velocity are represented, these pictures represent the flow state when a blade reaches the vertical position. It is interesting to note that the model handles well (1) the effect of rotation, (2) the velocity discontinuities, (3) the existence of strong vortical structures



DOI: 10.1002/fld

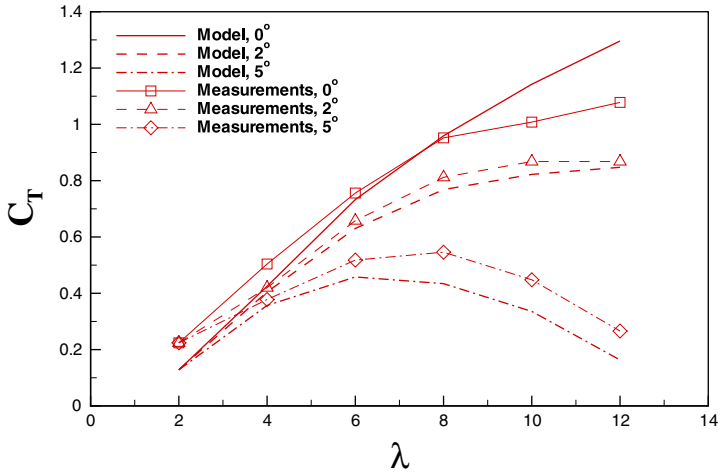


Figure 24. Thrust coefficient as a function of tip-speed ratio.

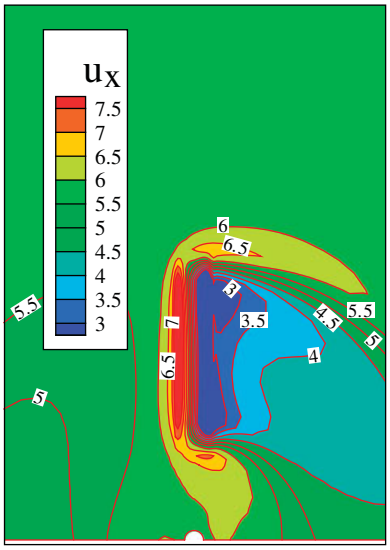


Figure 25. Axial component of $\mathbf{V}_{nr}$.

emanating from both the tip and root areas of the rotor and (4) the induction of the AS on the flow upstream of the rotor. Figure 26 is particularly striking and shows that the model can be used to trace tip vortex trajectories.

For the particular case of $\lambda = 8$, detailed experimental measurements have been obtained by TUDelft [28, 29] using hot-film anemometry, phase averaging and novel recombination methods to derive the 3D components of velocity. These measurements were taken both in the inflow and near-wake region of the turbine along planes parallel to the rotor swept surface. Figures 27–29



DOI: 10.1002/fld

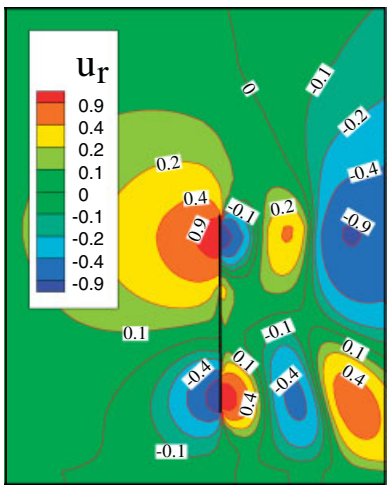


Figure 26. Radial component of $\mathbf{V}_{nr}$ flow is from left to right.

present comparisons at planes located $0.03D$, $0.05D$ and $0.075D$ (corresponding to 3.5, 6 and 9 cm) downstream of the rotor between the numerical results and the experimental measurements for the axial, tangential and radial components of the non-rotating velocity (in m/s). In each figure, three radial locations are presented: $r/R=0.4$ (blade root area), $r/R=0.7$ (mid-span area) and $r/R=0.9$ (blade tip area). Components of velocity are plotted against azimuthal position $\theta$.

It can be observed that a significant bias exists between experimental measurements and model outputs for the axial and radial components. However, it is remarkable that the shape of azimuthal distributions of velocity components are very similar between the model and the measurements, and that the rapid changes of the flow velocity components as a function of downstream distance is qualitatively well reproduced by the numerical solution. Furthermore, it may be noted that the bias between experimental and modeled components of velocity is, on the average, reduced with increasing axial distance from the rotor. From these observations, it seems questionable to calculate the blade loading through blade-element theory, as presented in Section 2.2. However, Figure 30 shows a comparison between experiments (taken from [28]) and model calculations for the axial component of velocity where the agreement is much better. Here, the rapid evolution of axial velocity at the tip and root of the AS raises questions as to the origin of these variations. As already observed in the case of the finite wing, this is typical of the AS representation and has to be linked to the bound vorticity along the AS.

These disagreements between the model and the experiments can be attributed to several factors, starting with the obvious differences between the object modeled by the AS within the CVFEM and the real wind turbine (which is not completely porous as the AS is). Another important factor concerns the effect of rotation on blade aerodynamics, which can dramatically change lift and drag characteristics, hence the circulation along a blade section when compared with 2D characteristics [31]. Similar to a blockage effect that is not taken into account by the model, the absence of a solid boundary to model the blades of the rotor most probably influences the numerical solution. In the central part of the rotor, the induced blockage effect might even be stronger since local blade solidity $c/r$ is higher. The uncertainties associated with the discretization (domain size



DOI: 10.1002/fld

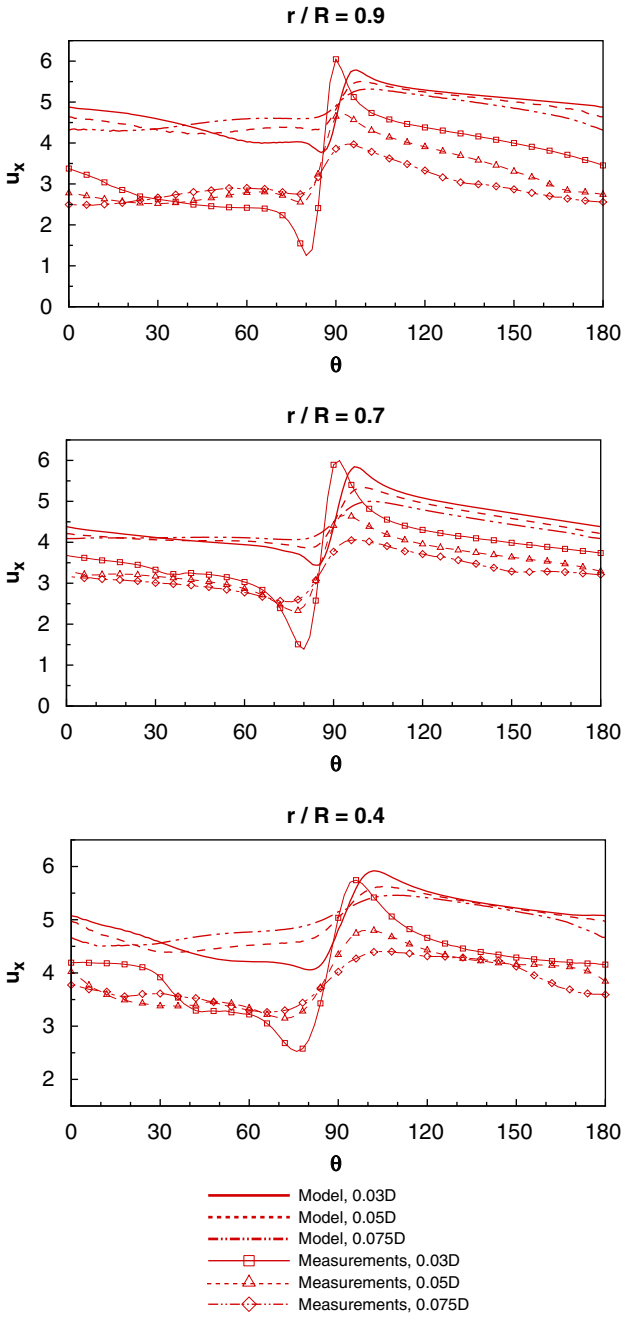


Figure 27. Axial component of $\mathbf{V}_{nr}$ as a function of azimuth for different radial locations.



DOI: 10.1002/fld

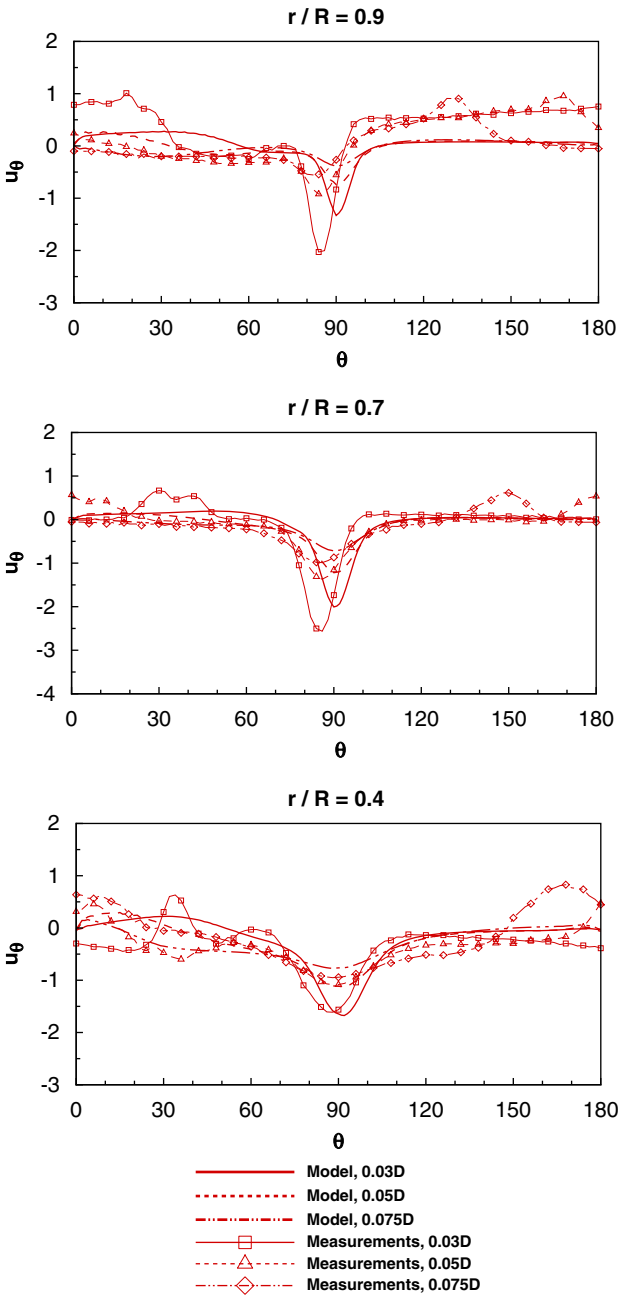


Figure 28. Tangential component of $\mathbf{V}_{nr}$ as a function of azimuth for different radial locations.



DOI: 10.1002/fld

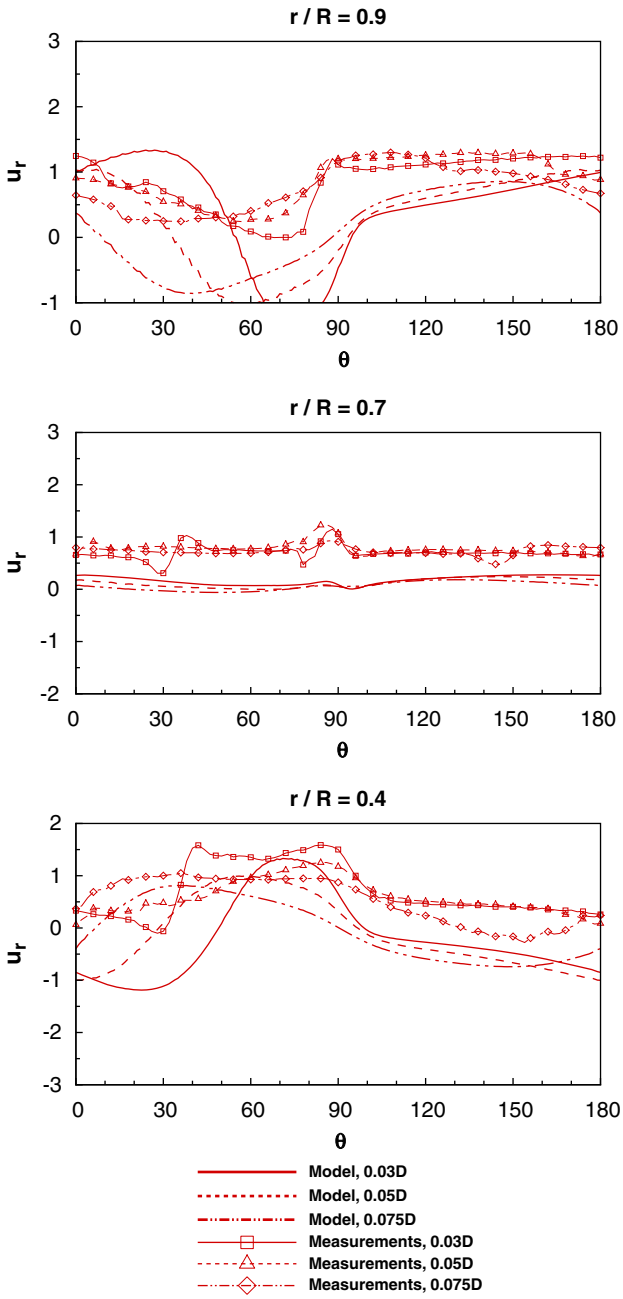


Figure 29. Radial component of $\mathbf{V}_{nr}$ as a function of azimuth for different radial locations.



DOI: 10.1002/fld

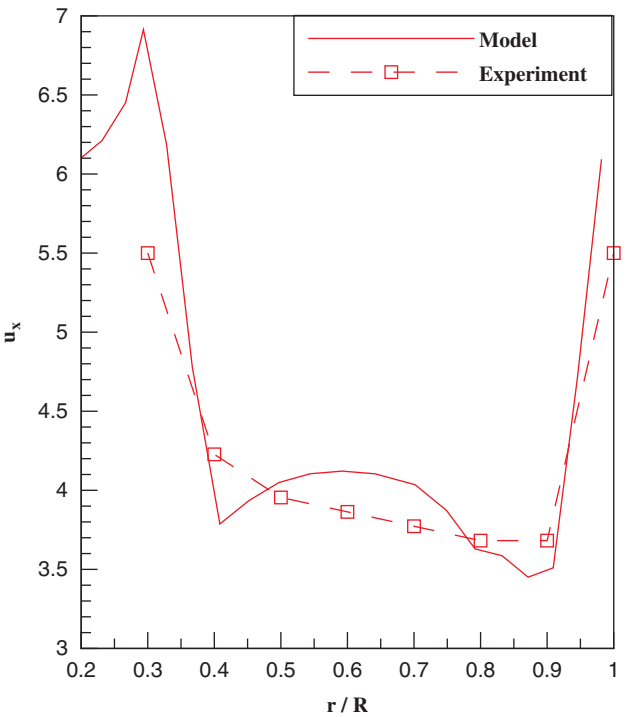


Figure 30. Radial distribution of axial velocity at the middle of the blade ($\theta = \pi/2$).

and mesh, convection model, numerical dissipation) and the treatment of boundary conditions are also cause for some of the observed discrepancies.

Finally, the AS method has recently been compared with other methods appropriate for wind turbine aerodynamics (blade-element momentum—BEM—and vortex methods). As regards rotor aerodynamics, the qualitative and quantitative comparisons performed show that the actuator surface concept agrees well with the other numerical models. The AS method has, however, the intrinsic advantages to model the blade tip vortices naturally, as well as their diffusion and evolution, whereas BEM or vortex methods must use *ad hoc*, empirical models. The AS method is envisioned to be useful for the study of the near- and far-wake aerodynamics, which is not satisfactorily modeled by BEM or vortex models with a lower cost in terms of computational costs than the full CFD models.

## 5. CONCLUSION

To model lifting devices, whether it be a wing in translation or rotation, this article proposes the concept of an actuator surface (AS) defined as a porous moving surface that carries velocity and pressure discontinuities as well as an induced system of forces. The origins and derivation of this concept have been reviewed to show that it respects conservation of vorticity and energy exchange accordingly with the onset of lift by ensuring constant total pressure in the reference frame fixed



DOI: 10.1002/fld

to the AS. 2D and 3D versions of a control volume finite-element model (CVFEM) are used to model the inviscid flow that results from this singular surface. The implementation of the AS action on the flow in these two methods was simplified by the integral approach of the CVFEM as regards the discretization of the Navier–Stokes equations. In addition to the modifications pertaining to the action of the AS, the specific adaptations to the 3D CVFEM for the study of flows in a non-inertial rotating frame of reference are also presented. The proposed model and numerical methods are then used to study the 2D and 3D inviscid flows of (i) a uniformly loaded segment, (ii) an actuator disk, (iii) a finite wing and (iv) a Wind Turbines. In the first two cases, the method appears to be accurate in the determination of the flow velocity and associated system of forces. In the case of the finite wing, for 24 different tapered wing planforms, the AS, which takes the shape of each wing planform, reproduces numerous characteristics of the flow (lift, induced drag and induced angle of attack) with good accuracy compared with the Prandtl lifting line model. A modified version of the AS is also used where velocity is not allowed to be discontinuous across the AS, but pressure is, in an attempt to reproduce the results of a model based on the distribution of volume forces. The results of this modified version show significant differences with the Prandtl lifting line lift and induced drag, which imply that volume force methods that impart all of their action on a single layer of nodes could be misguided. As a last application, the experimental wind turbine rotor of the Technical University of Delft is thoroughly analyzed. Comparisons between numerical model output and experimental measurements are presented for the power and thrust coefficients and for near-wake velocity measurements. The results are encouraging. The values of thrust coefficient calculated by the model are close to those observed in the experiments and it was found that details of the flow structure inherent to a vortical wake are well reproduced by the proposed model. These are good signs that the model should be appropriate to analyze wake evolution of rotating lifting bodies like propellers, helicopters and Wind Turbines. Further developments and case studies are needed to study the influence of the AS loading distribution on the flow and the relative performance of this new concept versus classical concepts (vortex, actuator-disk, volume force-based methods). On a fundamental level, the integration of viscous drag in the flow model is also a subject of interest.

## ACKNOWLEDGEMENTS

We would like to thank TUDelft for providing access to their experimental data. This study received support from the Canada Research Chairs Program. Support from the Natural Sciences and Engineering Research Council of Canada (NSERC) in the form of research grants is gratefully acknowledged.

## REFERENCES

1. Meyer C, Kröger D. Numerical simulation of the flow field in the vicinity of an axial flow fan. *International Journal for Numerical Methods in Fluids* 2001; **36**:947–969.
2. Tahara Y, Tohyama S, Katsui T. CFD-based multi-objective optimization method for ship design. *International Journal for Numerical Methods in Fluids* 2006; **52**:499–527.
3. Leishman J. *Principles of Helicopter Aerodynamics*. Cambridge Aerospace Series. Cambridge University Press: Cambridge, 2000.
4. Chaffin M. A guide to the use of the pressure disk rotor model as implemented in INS3D-UP. *Technical Report NASA CR-4692*, NASA, 1995.
5. Wagner S. Flow phenomena on rotary wing systems and their modeling. *ZAMM Journal of Applied Mathematics and Mechanics* 1999; **79**:795–815.



DOI: 10.1002/fld

6. Boyd D. Rotor/fuselage unsteady interactional aerodynamics: a new computational model. *Ph.D. Thesis*, Virginia Polytechnic Institute and State University, 1999.
7. Sørensen J, Shen W. Numerical modeling of wind turbine wakes. *Journal of Fluids Engineering* 2002; **124**: 393–399.
8. Masson C, Smaili A, Ammara I, Leclerc C. Aerodynamic investigations on tower shadow impacts for HAWTs. *Proceedings of the ASME Wind Energy Symposium*, American Institute of Aeronautics and Astronautics (2000-0041), Reno, NE, 2000.
9. Breslin J, Andersen P. *Hydrodynamics of Ship Propellers*. Ocean Technology Series 3. Cambridge University Press: Cambridge, 1994.
10. Wu JZ, Ma HY, Zhou MD. *Vorticity and Vortex Dynamics*. Springer: Berlin, 2006.
11. Batchelor G. *An Introduction to Fluid Dynamics*. Cambridge University Press: Cambridge, 2000.
12. Panton R. *Incompressible Flow*. Wiley: New York, 2005.
13. Schmitz S, Chattot JJ. Flow physics and Stokes' theorem in wind turbine aerodynamics. *Computers and Fluids* 2007; **36**:1583–1587.
14. Shen WZ, Zhang JH, Sørensen JN. The actuator surface model: a new Navier–Stokes based model for rotor computations. *Journal of Solar Energy Engineering* (ASME) 2009; **131**(1):011002.
15. Dobrev I, Massouh F, Rapin M. Actuator surface hybrid model. *Proceedings of the Science of Making Torque from Wind* (*2nd conference*), Journal of Physics: Conference Series, Danish Technical University, DK, 2007.
16. Masson C, Saabas H, Baliga B. Co-located equal order control volume finite element method for two-dimensional axisymmetric incompressible fluid flow. *International Journal for Numerical Methods in Fluids* 1994; **18**:1–26.
17. Saabas H. Control volume finite element method for three-dimensional, incompressible, viscous fluid flow. *Ph.D. Thesis*, Mc Gill University, 1991.
18. Tran LD, Masson C, Smaili A. A stable second-order mass-weighted upwind scheme for unstructured meshes. *International Journal for Numerical Methods in Fluids* 2005; **51**:749–771.
19. Patankar SV. *Numerical Heat Transfer and Fluid Flow*. Series in Computational and Physical Processes in Mechanics and Thermal Sciences. Mcgraw-Hill: New-York, 1980.
20. VanKuik G. The edge singularity of an actuator disc with a constant normal load. *Proceedings of the ASME Wind Energy Symposium*, American Institute of Aeronautics and Astronautics (2003-0356), Reno, NE, 2003.
21. Conway J. Exact actuator disk solutions for non-uniform heavy loading and slipstream contraction. *Journal of Fluid Mechanics* 1998; **365**:235–267.
22. Hansen A, Butterfield C. Aerodynamics of horizontal-axis wind turbines. *Annual Review of Fluid Mechanics* 2000; **25**:115–149.
23. Leclerc C, Masson C. Wind turbine performance predictions using a differential actuator-lifting disk model. *Journal of Solar Energy Engineering* (ASME) 2005; **127**(2):200–208.
24. Rajagopalan R, Fanucci J. Finite difference model of vertical axis wind turbines. *Journal of Propulsion and Power* 1985; **1**(6):432–436.
25. Masson C, Ammara I, Paraschivoiu I. An aerodynamic method for the analysis of isolated horizontal-axis wind turbines. *International Journal of Rotating Machinery* 1997; **3**:21–32.
26. Sørensen J, Myken A. Unsteady actuator disk model for horizontal axis wind turbines. *Journal of Wind Engineering and Industrial Aerodynamics* 1992; **39**:139–149.
27. Anderson J. *Fundamentals of Aerodynamics*. McGraw-Hill Science: New York, 2005.
28. Sant T. Improving BEM-based aerodynamic models in wind turbine design codes. *Ph.D. Thesis*, Technical University of Delft, 2007.
29. Haans W, Sant T, Van Kuik G, Van Bussel G. HAWT near-wake aerodynamics. Part I: axial flow conditions. *Wind Energy* 2008; **11**(3):245–264.
30. Sheldahl RE, Klimas PC. Aerodynamic characteristics of seven airfoil sections through 180 degrees angle of attack for use in aerodynamic analysis of vertical axis wind turbines. *Technical Report SAND80-2114*, Sandia National Laboratories, 1981.
31. Schreck S, Robison M. Rotational augmentation of horizontal axis wind turbine blade aerodynamic response. *Wind Energy* 2002; **5**:133–150.




DOI: 10.1002/fld